MASTERARBEIT / MASTER'S THESIS

Titel der Masterarbeit / Title of the Master's Thesis

„Magnetoresistive sensor elements with perpendicular anisotropy"

verfasst von / submitted by

Amil Ducevic, BSc

angestrebter akademischer Grad / in partial fulfilment of the requirements for the degree of

Master of Science (MSc)

Wien, 2019 / Vienna, 2019

Studienkennzahl lt. Studienblatt / degree programme code as it appears on the student record sheet:	UA 066 876
Studienrichtung lt. Studienblatt / degree programme as it appears on the student record sheet:	Masterstudium Physik
Betreut von / Supervisor:	Assoz. Prof. Dipl.-Ing. Dr. techn. Dieter Süss, Privatdoz.

Abstract

Magnetoresistance effects are becoming one of the most important magnetic sensor technologies for a wide variety of applications, e.g. the automotive industry and biomedical applications. Within this master thesis simulation results for magnetoresistance sensors utilizing perpendicular anisotropy with an emphasis on angle-sensing are presented. Basically all magnetoresisitve sensors currently on the market are sensitive to magnetic fields in plane of the magnetic material, therefore the basic idea in this work is to compensate the shape anisotropy, which is caused by the elongated form of the sensor, with a perpendicular anisotropy in order to obtain a smooth hysteresis curve for a field applied along the perpendicular axis.

The tool with which this is analyzed is micromagnetics. Micromagnetics has been applied to applications such as magnetic storage, magnetic sensors and more with great success. Hence embedding micromagnetism into a finite difference code is an eligible method to model this concept.

The first part is focused on the physics behind these sensing devices and how such materials are simulated using state of the art finite difference micromagnetic code, whereas the second part presents the simulation results. We find that a sensor as described above, can yield linear transfer curves, making it an attractive option for linear field sensors. Additionally if this sensor concept is implemented as an angle sensor its performance is comparable to state-of-the-art Hall angle sensing devices. However the performance is highly dependent on the position of the sensor.

Since the field of perpendicular magnetic anisotropy in sensors is still emerging new concepts provide challenges as well as opportunities, therefore the aim of this work is to present promising new sensor designs that provide an attractive alternative to current concepts.

Kurzfassung

Magnetoresistive Effekte entwickeln sich zu einer der wichtigsten magnetischen Sensortechnologien für eine Vielzahl von Anwendungen, z.B. in der Automobilindustrie oder in biomedizinischen Anwendungen. Diese Masterarbeit stellt Simulationsergebnisse für magnetoresistive Sensoren mit senkrechter Anisotropie mit Schwerpunkt auf Winkelmessungen vor. Alle derzeit auf dem Markt erhältlichen magnetoresistiven Sensoren sind empfindlich gegenüber Magnetfeldern in der Ebene des magnetischen Materials, daher besteht die Grundidee dieser Arbeit darin, die durch die längliche Form des Sensors verursachte Formanisotropie mit einer senkrechten Anisotropie zu kompensieren, um eine glatte Hysteresekurve senkrecht zur Sensorebene zu erhalten.

Das Werkzeug zur Analyse ist der Mikromagnetismus. Mikromagnetismus wurde mit großem Erfolg in Anwendungen wie magnetischen Speichermedien oder magnetischen Sensoren eingesetzt. Daher ist die Einbettung des Mikromagnetismus in einen finiten Differenzcode eine geeignete Methode, um dieses Konzept zu modellieren.

Der erste Teil konzentriert sich auf die Physik hinter diesen Sensoren und wie solche Materialien mit finiter Differenz unter Verwendung von fortgeschrittenem mikromagnetischem Code simuliert werden kann, während der zweite Teil die Simulationsergebnisse präsentiert. Wir stellen fest, dass ein Sensor, wie oben beschrieben, lineare Transferkurven liefern kann, was ihn zu einer attraktiven Option für lineare Feldsensoren macht. Wird dieses Sensorkonzept zudem als Winkelsensor realisiert, ist seine Performance mit den modernsten Hall-Winkelsensoren vergleichbar. Jedoch ist dies stark von der Position des Sensors abhängig.

Da sich das Feld der senkrechten magnetischen Anisotropie in Sensoren noch in der Entwicklung befindet, bieten neue Konzepte sowohl Herausforderungen als auch Chancen. Das Ziel dieser Arbeit ist vielversprechende neue Sensordesigns zu präsentieren, die eine attraktive Alternative zu bestehenden Konzepten bieten.

Contents

List of symbols and default values

Unless specifically stated otherwise the following symbols were used

Symbol	Description	Unit
$\vec{H}$, $\mu_0\vec{H} = \vec{B}$	Magnetic Field, Magnetic flux density	A/m, T
$\vec{M}$, $\mu_0\vec{M} = \vec{J}$	Magnetization, Polarization	A/m, T
M_s, $\mu_0 M_s = J_s$	Saturation magnetization, Saturation polarization	A/m, T
$\frac{\vec{M}}{M_s} = \vec{m}$	Normalized magnetization	1
A	Exchange constant	J/m
k_1 ,k_2, k_s	Magnetic anisotropy constant	J/m^3

Table 1: List of symbols frequently used in this thesis

Symbol	Description	Value
μ_0	Vacuum permeability	$4\pi \cdot 10^{-7} Vs/Am$
$\hbar$	Reduced Planck constant	$1.054571817... \cdot 10^{-34} Js$
e	Elementary charge	$1.602176634 \cdot 10^{-19} C$
m_e	Electron mass	$9.10938356 \cdot 10^{-31} kg$

Table 2: List of physical constants used in this thesis

Unless specifically stated otherwise, the free layer materials of the micromagnetic simulations can assumed to be Cobalt-Iron-Boron (CoFeB) or Cobalt-Platin multilayers (Co/Pt), both materials can be used for both perpendicular sensor designs which are introduced in this thesis.

Parameter	Description	Value
$\mu_0 M_S$	Saturation magnetization	$1.58T$
A	Exchange constant	$1.5 \cdot 10^{-11} J/m$

Table 3: Micromagnetic parameters for CoFeB, the values are taken from [39]

Parameter	Description	Value
$\mu_0 M_S$	Saturation magnetization	$1.82T$
A	Exchange constant	$3.1 \cdot 10^{-11} J/m$

Table 4: Micromagnetic parameters for Co, the values are taken from [21]

Chapter 1

Magnetism

The phenomenon of magnetism has engaged the interest of scientists for millennia. The ancient Greeks were already familiar with the mysterious force which seemed to only have an effect on iron. The Chinese were the first to discover an application in the form of a compass between 300 and 200 BC, although it hadn't been used in navigation purposes until 1000 AD[17].

Scientific research in a more modern sense, began in the renaissance with William Gibert. Gibert found that the function of the compass is based on the magnetic field the earth generates. An understanding of the relationship between magnetism and electricity started to form in 1819 with Hans Christian Ørsted. He discovered by accident that an electric current can create a magnetic field when he noticed the twitching of a compass needle near an electric wire. Another breakthrough came from Andre-Marie-Amper, who came to the conclusion that a magnetic field is created by charges in motion, these charges were later characterized as electrons. Additional discoveries were made by scientists like Carl-Friedrich Gauss, Jean-Baptiste Biot, Felix Savart and Michael Faraday, which further connected electricity to magnetism. James Clark Maxwell gathered these insights by his colleagues and synthesized them into Maxwell's equations, which describe how electric- and magnetic fields are connected with each other and with electric charges and currents under certain boundary conditions. They are a system of linear partial differential equations that connect electricity, magnetism and optics into the field of electromagnetism.

A fundamental aspect of magnetism was discovered independently by Niels Bohr and J.H van Leuwen. In their respective doctoral theses [18,19] it is shown that the phenomena of magnetism is heavily connected to quantum mechanics. The Bohr-van Leeuwen theorem states that in a uniform magnetic field and in thermal equilibrium, the magnetization of an electron gas in the classic Drude-Lorentz model vanishes. Which means that a classical electron system cannot have a magnetization when in thermal equilibrium, therefore magnetism is a quantum mechanical phenomenon.

1.1 Magnetization, magnetic moment and Spin

The state of a magnet is described in terms of its magnetization $\vec{M}(\vec{r})$ which is defined as the magnetic dipole-moment $\vec{m}_d$ per volume V

$$\vec{M} = \frac{\vec{m}_d}{V} \tag{1.1}$$

The magnetic moment $\vec{m}_d$ is given by

$$\vec{m}_d = \sum_i \vec{\mu}(\vec{r_i}) = \sum_i -g\frac{|e|}{2m_e}\hbar\vec{S}(\vec{r_i}) = \sum_i -g\mu_B\vec{S}(\vec{r_i}) \tag{1.2}$$

here $\vec{\mu}(\vec{r_i})$ is the local magnetic moment of an atom or ion at the position $\vec{r_i}$, g is the Lande factor ($g \approx 2$ for metal systems with quenched orbital moment), μ_B is the Bohr magneton, e is the charge of the electron, m_e is the electron mass and $\hbar\vec{S}(\vec{r_i})$ is the spin angular momentum, where $\hbar$ is the reduced Planck constant.

The length of the magnetization is independent of the strength of the external field $|\vec{H}(\vec{r})|$, the length depends on the temperature T

$$|\vec{M}| = M_s(T) = M_s \tag{1.3}$$

The temperature T is constant over the entire ferromagnetic body in micromagnetism.

1.2 Magnetic hysteresis

If the magnetization of a ferromagnetic material is driven to saturation by an external field, it will not go back to zero once the field is removed. The amount of magnetization that it retains at zero field is called its remanence. In order to drive the magnetization back to zero one needs to apply the field in the opposite direction, the amount of field that is needed to completely demagnetise the ferromagnetic body is called its coercivity. If alternating fields are applied to this material, the magnetization will draw out a loop called a hysteresis loop. A significant number of literature, e.g. [2,8,22] explains hysteresis with the creation and annihilation of magnetic domains. However the Stoner-Wolfarth model, which will be discussed in detail later on, also predicts hysteresis, this is particularly surprising since the stonar-wolfarth model describes macroscopic magnetic materials as if they are single spins with a certain anisotropy axes, meaning there are no magnetic domains.

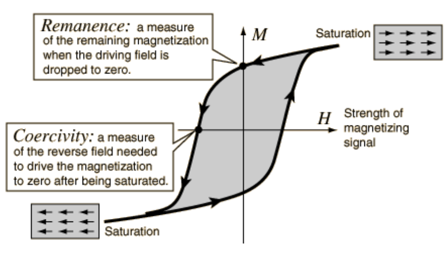

Figure 1.1: The hysteresis curve. Figure taken from [22]

1.3 Magnetic sensing

There are many ways to measure magnetic fields, most of them are based on the fundamental connection between magnetic and electric phenomena. There is a wide variety of different concepts and technologies exploiting this connection. The respective technology used for an application depends mostly on the expected field magnitude and range. Figure 1.2 gives a visualization of the sensing regimes for different magnetic sensor technologies. Sensors based on the Hall-effect

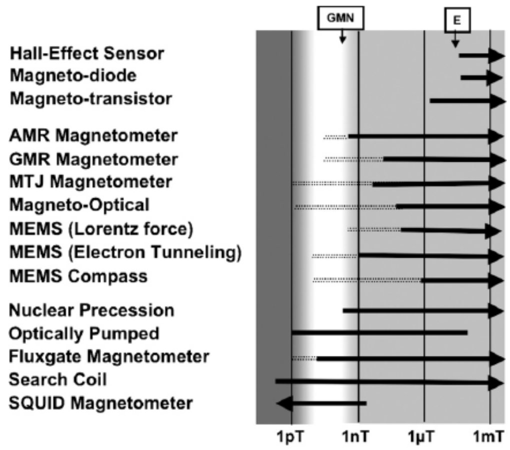

Figure 1.2: Sensing regimes for various magnetic sensor technologies. The marks 'E' and 'GMN' indicate the strength of Earth's magnetic field and geomagnetic noise respectively. Figure taken from [23]

are still widely used for wheel speed sensing but they are slowly being replaced in parts by magnetoresistive technologies, this is due to their accuracy. For instance the detectivity, which is the smallest difference in magnetic field which a sensor can register, that Hall sensors exhibit is of $100\,nT/\sqrt{Hz}$ whereas magnetoresisitive technologies exhibit detectivities of $1\,nT/\sqrt{Hz}$[28].

An essential characteristic of not only magnetic sensors but all magnetic materials are the $M(H)$ curves for a periodically alternating field $\vec{H}$ along an axis. The $M(H)$ curve depends heavily upon the application. For instance a permanent magnet is required to have hard magnetic characteristics like high remanence and coercitivity, since one wouldn't want the permanent magnet to change its magnetization too easily. The $M(H)$ curve for magnetic sensing devices is also referred to as the transfer curve. The ideal transfer curve can vary from sensor to sensor, for our application the transfer curve should have soft magnetic characteristics, meaning that the remanence and coercitivity are close to zero. A soft magnetic material exhibits no hysteresis, making the transfer curve a bijective function, therefore one could form the inverse and a given sensor readout value for M would therefore unambiguously correspond to a field value H.

1.4 Magnetoresistive effects

In this thesis an emphasis is put on magnetic sensors that exploit the giant magnetoresistance (GMR) and tunneling magnetoresistence (TMR) effect. The GMR effect was discovered int the late 1980s independently by Albert Fert [25] et al. and Peter Gruenberg et al. [27] and earned both of them the 2007 Nobel Prize in Physics. Both noticed very large resistance changes in materials comprised of alternating very thin layers of various metallic elements. The effect in itself was not unheard of, since the anisotropic magnetoresistance (AMR) had been well known since 1856 when it was discovered by Lord Kelvin. However GMR yielded significantly higher changes in the resistance, hence the effect was labeled 'giant'.

GMR and TMR devices have a basic common structure: two ferromagnetic metal films which are seperated by a nonmagnetic film. In the case of GMR that nonmagnetic film is a metal film, whereas with TMR we have an insulator film. The electric resistance R of these devices depends on the relative directions between the magnetization of both ferromagnetic films. If a magnetic field $\vec{H}$ were to be applied it would cause a change in the direction of one ferromagnetic film, the resistance R would therefore also change and thus showing the magnetoresistance (MR) effect, as seen in figure 1.2d. The magnetoresistance ratio is given by

$$\chi = \frac{R^{\uparrow\downarrow} - R^{\uparrow\uparrow}}{R^{\uparrow\uparrow}} \tag{1.4}$$

$R^{\uparrow\uparrow}$ and $R^{\uparrow\downarrow}$ indicate the resistances for the two magnetizations in parallel and in antiparallel.

1.4.1 Physics of GMR and TMR devices

Conductivity of a ferromagnetic metal(Two-Current-Model)

In nonmagnetic metals conduction electron are scattered by imperfections such as phonons or lattice defects and the resistivity can be written as

$$\rho(T) = \rho + \rho_0(T) \tag{1.5}$$

where the temperature independent term ρ_0 is the resistivity which is based on scattering by impurities and lattice defects and the second term $\rho_0(T)$ is temperature dependent and due to scattering by thermal phonons.

In ferromagnetic materials, however, the electrons are further scattered by magnons and by magnetic impurities, which originate in interactions between magnetic moments of these scattering centers and spins of conduction electrons. Electrons with spin parallel to the total magnetization of the ferromagnetic metal, namely electrons with majority spin are indicated by $\uparrow$, whereby electrons antiparallel to the magnetization are called electron with minority spins and are denoted by $\downarrow$. At temperatures significantly below the Curie-point T_C magnon scattering becomes negligibly small and the majority and minority $\downarrow$ spins don't mix with each other [24] during the scattering process. The electric current is therefore carried by electrons with $\uparrow$ and $\downarrow$ independently and therefore the conductivity σ is expressed by

$$\sigma = \sigma^{\uparrow} + \sigma^{\downarrow} \quad \sigma^{\uparrow,\downarrow} = e^2 \tau^{\uparrow,\downarrow} n^{\uparrow,\downarrow}/m^* \tag{1.6}$$

here e is the electron charge, m^* is the effective mass $\tau^{\uparrow,\downarrow}$ is the relaxation time for the electrons and $n^{\uparrow,\downarrow}$ is the density of conduction electrons with majority and minority spin respectively. Due to exchange interaction between the d-electrons the majority spin $d^{\uparrow}$-band and the minority $d^{\downarrow}$-band shift relative to each other. The $d^{\uparrow}$-band shifts down by ϵ_x and the Fermi energy ϵ_F is located above the $d^{\uparrow}$-band and vice versa for the $d^{\downarrow}$-band as shown in figure 1.3(a). Conduction electrons belonging to the $s^{\downarrow}$-band are being scattered by magnetic impurities to the $d^{\downarrow}$-band, where electrons have a bigger effective mass m^* and contribute slightly to the electric conduction, whereas electrons from the $s^{\uparrow}$ don't scatter to the $d^{\uparrow}$ band due to the completely filled $d^{\uparrow}$-band at ϵ_F. This means that $\tau^{\downarrow} < \tau^{\uparrow}$ and therefore conductance asymmetry occurs, with the asymmetry factor

$$\alpha = \frac{\sigma^{\uparrow}}{\sigma^{\downarrow}} > 1 \tag{1.7}$$

Calculated energy bands and tables with asymmetry factors α for 3d-transition metals can be looked up in [24].

GMR devices

The electron trajectory for $\uparrow$(spin-up) and $\downarrow$(spin-down) electrons are shown schematically in figure 1.3(b). If the electron spin differs from the magnetization of the passing layer, the conduction electron are scattered more strongly and vice versa.

A typical GMR device is a spin valve with a structure similar to the one shown in figure 1.3 (c). It is made up of a ferromagnetic layer (PL) with pinned magnetization, another ferromagnetic layer

(FL) with free magnetization and a nonmagnetic spacer layer (SL) for separating magnetically both ferromagnetic layers. If an external magnetic field $\vec{H}$ is applied, the magnetization $\vec{M}_{PL}$ of the pinned layer wouldn't change due to the adjacent antiferromagnetic layer (AL) but the magnetization $\vec{M}_{FL}$ changes its direction dependent on how $\vec{H}$ is applied.

Simple model for TMR ratio

A TMR device looks like the structure shown in figure 1.3(c) except that the nonmagnetic spacer layer (SL) is replaced by an insulator film (I), this structure is also called ferromagnetic tunnel junction, in other words a ferromagnetic tunnel junction is composed of two ferromagnetic electrodes (1) and (2) separated by an insulator film (I). We assume that the separator film (I) has a square barrier potential U, thickness t, and the magnetization of both electrodes $\vec{M}_1$, $\vec{M}_2$. Tunnel currents flow from (2) to (1) if a voltage is applied between (2) and (1) but at low temperatures these currents can again be considered independently, where they consist of two components ↑-spin electron and ↓-spin electrons.

Figure 1.3(e) shows the electron energy configurations for parallel and antiparallel alignment in the junction. The Fermi level of (1) ϵ_f is lowered by eV relatively to electrode (2) and the barrier height U_0 is higher than the Fermi-level ϵ_f. The conduction electrons have approximately kinetic energies which correspond to ϵ_F and tunnel through the barrier conserving their spins. In the case of parallel alignment the electric conductance of the tunnel junction is given by

$$\sigma_T^{\uparrow\uparrow} \propto exp(-AU_0^{1/2})[D_1^{\uparrow}(\epsilon_F)D_2^{\uparrow}(\epsilon_F + eV) + D_1^{\downarrow}(\epsilon_F)D_2^{\downarrow}(\epsilon_F + eV))] \tag{1.8}$$

where the exponential factor on the right hand side is the tunneling probability of the electrons and $D_{1,2}^{\uparrow}$ and $D_{1,2}^{\downarrow}$ are the state densities for ↑- and ↓- spin electrons. For the antiparallel case the ↑-spin electrons move through the barrier form the majority band of electrode (1) to the minority band of electrode (2) and vice versa therefore the conductance is

$$\sigma_T^{\uparrow\uparrow} \propto exp(-AU_0^{1/2})[D_1^{\uparrow}(\epsilon_F)D_2^{\downarrow}(\epsilon_F + eV) + D_1^{\downarrow}(\epsilon_F)D_2^{\uparrow}(\epsilon_F + eV))] \tag{1.9}$$

Now we can calculate the TMR ratio

$$\chi := (\sigma_T^{\uparrow\uparrow} - \sigma_T^{\uparrow\downarrow})/\sigma_T^{\uparrow\downarrow} = 2(D_1^{\uparrow} - D_1^{\uparrow})(D_2^{\uparrow} - D_2^{\uparrow})/(D_1^{\uparrow}D_2^{\downarrow} + D_1^{\downarrow}D_2^{\uparrow}) = 2P_1P_2/(1 - P_1P_2) \tag{1.10}$$

with $P_i = (D_i^{\uparrow} - D_i^{\downarrow})/(D_i^{\uparrow} - D_i^{\downarrow})$, $i = 1, 2$ and is determined by the polarization P_1 and P_2 of the ferromagnetic electrodes. This relation was found by Julliere[29] and was later confirmed by Maekawa[30].

1.4.2 Vortex sensor

The vortex sensor is a fairly recent concept introduced by D.Suess et.al.[26] and was introduced as a way to overcome the limitation of the (at that time) state of the art magneto resistance sensors, e.g magnetic noise or a nonlinear hysteresis curves. This work will only use the vortex sensor as a comparison when examining the performance of the sensor concepts which are at the heart of this work. Therefore this section is supposed to give a short description of the vortex sensor.

In thin ferromagnetic discs no direction in the plane of the disc is energetically favourable to any other for the magnetization $\vec{M}$, assuming there is no external field $\vec{H}$. If the ratio between the disk diameter D and the thickness t is within a certain range, the magnetic ground state may be a vortex state, which means that the magnetic moments are aligned in concentric circles a around a core, which is located in the centre of the disc, where the magnetization points out of the plane. The symmetry of this system already gives 4 energetically equivalent states, since there are 2 different directions for the core and the concentric circles respectively.

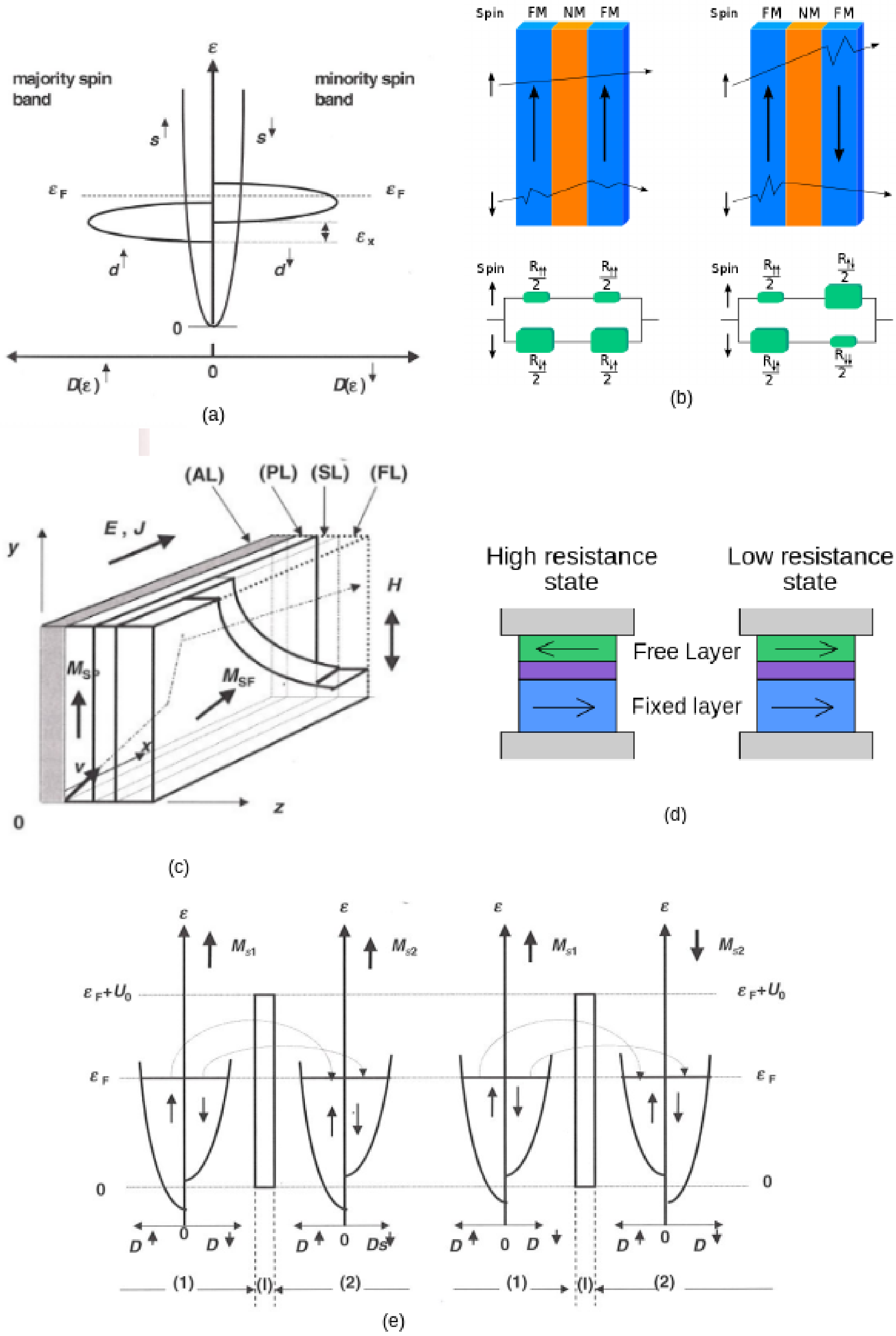

Figure 1.3: (a) Schematic presentation of spin-polarized energy-bands in a ferromagnetic metal.(b)Schematic for the two-currrent model of the GMR-effect, with a parallel circuit with branches for spin-up spin-down current (c)Schematic presentation of a spin valve, where (AL) is antiferromagnetic layer,(PL) a pinned magnetization layer,(SL) a nonmagnetic spacer layer and (FL) a free magnetization layer (d)Schematic for a current magnetoresitive device. The magnetization of the easy layer can be tilted easily if an external field is applied, while the magnetization of the fixed layer remains unchanged (e) Schematic representation of the relevant energy-bands for magnetic tunnel junctions. Figures taken from [24,28]

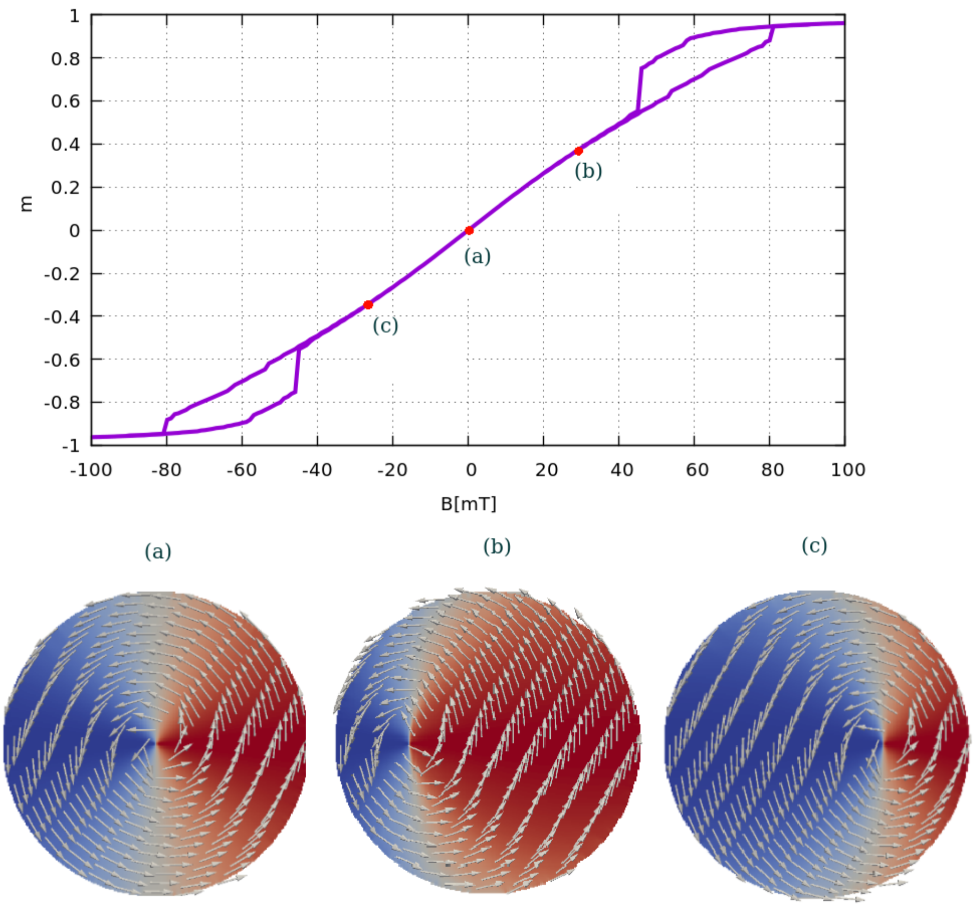

Figure 1.4: Hystereses of a vortex sensor with corresponding magnetization configurations at specific points of the hysteresis

Applying an in plane field $\vec{H}$ to a vortex state will displace the vortex core. The displacement happens in such a manner, that magnetic moments parallel to the external field $\vec{H}$ are increased and magnetic moments anti-parallel to the external field are decreased, as shown in figure 1.4. Figure 1.4 was simulated with parameters for a CoFeB alloy with $t = 1.3nm$ and $D = 800nm$.

Chapter 2

Magnetic anisotropy

A characteristic property of magnetic materials is their anisotropy, which means that certain magnetization directions are preferred, we call these easy axis and that others are avoided, these are referred to as hard axis, as can be seen in Figure 2.1. These easy axes are undirected, meaning that the energy does not depend on the sign of the magnetization:

$$E_{ani}(\vec{m}) = E_{ani}(-\vec{m}) \tag{2.1}$$

The crystal anisotropy energy E_{ani} is the work which needs to be done by the external influences in order to move the magnetization away from the easy axis. The functional form of the energy can be obtained phenomenologically. Typical anisotropy energy densities, also known as anisotropy constants k can vary from $0.05MJ/m^3$ for bcc Fe and $0.5MJ/m^3$ for hcp Co to $10.0MJ/m^3$ for rare-earth magnets[2]. Depending on which type of anisotropy is considered, the physical origin of the anisotropy can vary, e.g. the magneto crystalline anisotropy, has its origins mainly in the spin-orbit interaction, while other anisotropies are linked to induced anisotropies like shape-, or magneto-elastic anisotropies. However the macroscopic contributions are quite similar, which will be the topic of this section.

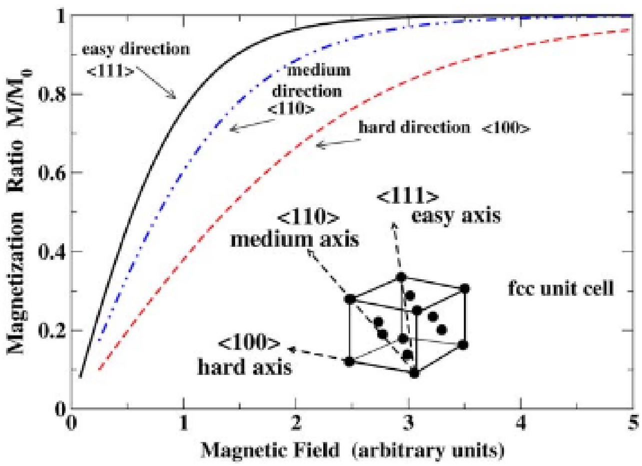

Figure 2.1: Schematic of various possible axis which can be magnetized for a fcc crystal. Here (111) is the easy axes, while (100) is the hard axis. Figure taken from [7]

2.1 Crystalline anisotropy

The origin of crystalline anisotropy lies in spin orbit coupling and crystal field interaction.In solids the spin orbit coupling and the crystal-field splitting compete with each other. The latter favours the suppression(quenching) of the orbital moment. Quenched orbitals tend to have more standing wave-character and adapt more easily to the crystal-field than unquenched wave orbitals. The result of this competition determines the degree of the orbital quenching and the magnitude of the anisotropy. 3d electrons tend to have strong quenching, e.g. iron has a magnetization of 2.2 μ_B, where only roughly 5% of this moment stem from the orbit. 4f electrons in rare earth ions, on the other hand, are close to the nucleus and therefore combine a weak crystal-field interaction with a strong spin orbit coupling. This short section was only meant to briefly discuss the origin of crystalline anisotropy for completeness sake, for a full derivation see [2]. The rest of this chapter will deal with anisotropy in a more phenomenological way.

2.1.1 Uniaxial Anisotropy

Magnetic materials which exhibit a hexagonal or tetragonal crystal structure can be considered isotrope in a plane which is perpendicular to a certain axis with direction $\vec{u}$. This is valid for crystal structures which have one single axis of high symmetry, in this case we are talking about uniaxial anisotropy. If we consider the axis to be parallel to the z-axis in spherical coordinates we can denote the energy density e_{ani} as

$$e_{ani} = k_1 sin^2\theta + k_2 sin^4\theta + ... \tag{2.2}$$

where k_1, k_2 are the first and second order uniaxial anisotropy constants and θ is the angle between the easy axis and the magnetization. Orders higher than 4 were ignored and odd order terms are not included due to (2.1). This simple anisotropy-energy expression was derived by Neel[1],it may be simple but it is nonetheless a powerful parametrization of the magnetic anisotropy. For $K_1 > 0$ the energy has a minimum at $\theta = 0$ and $\theta = \pi$, so that the easy axis is parallel to the symmetry axis. If $K_1 < 0$ the energy minimum is at $\theta = \pi/2$, which means the magnetization is free to rotate in the plane, which is known as easy-plane anisotropy. Figure 2.2 (a,b) shows areas of constant energy density for uniaxial anisotropy. The crystalline anisotropy energy is then given by

$$E_{ani} = \int_V e_{ani}(\vec{m})dV \tag{2.3}$$

where the integral goes over the volume V of the magnetic body in question.

2.1.2 Cubic anisotropy

For a cubic system one can denote the contribution of the crystalline anisotropy to the free energy density as

$$e_{ani} = k_0 + k_1(m_x^2 m_y^2 + m_y^2 m_z^2 + m_z^2 m_x^2) + k_2(m_x^2 m_y^2 m_z^2) + ... \tag{2.4}$$

The first term on the right hand side can be dropped since it does not depend on $\vec{m}$ and we are only interested in the change of energy, additionally one can drop the sixth order term, since terms with $k_2 > 0$ are only relevant if the magnetization favors easy axis along the diagonals of the cube too, which is not relevant to this thesis. This leaves

$$\begin{gathered} e_{ani} \approx k_1(m_x^2 m_y^2 + m_y^2 m_z^2 + m_z^2 m_x^2) = \\ k_1[(\vec{a}\cdot\vec{m})^2(\vec{b}\cdot\vec{m})^2 + (\vec{b}\cdot\vec{m})^2(\vec{c}\cdot\vec{m})^2 + (\vec{c}\cdot\vec{m})^2(\vec{a}\cdot\vec{m})^2] \end{gathered} \tag{2.5}$$

whereby $\vec{a}, \vec{b}$ and $\vec{c}$ are the unit vectors along the axes of a cubic crystal. It is quite obvious that for $k_1 > 0$ e_{ani} is minimal if the magnetization is parallel to one of the three axes, meaning the easy axis for a cubic system are along the vectors $\vec{a}, \vec{b}, \vec{c}$ if $k_1 > 0$. Figure 2.2 (c,d) shows areas of constant energy density for cubic anisotropy. The anisotropy energy E_{ani} can again be calculated by (2.3)

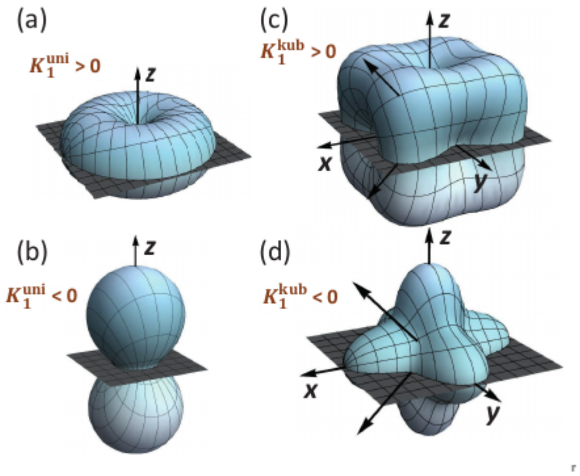

Figure 2.2: Surfaces of constant energy density for uniaxial anistropy with $k_1 > 0$(a),$k_1 < 0$(b) and for cubic anisotropy with $k_1 > 0$(c),$k_1 < 0$(d). Only the first order terms were taken into consideration. Figure taken from [8]

2.2 Shape anisotropy

Shape or dipolar anisotropies have their origin in magnetostatic interaction between pairs of magnetic dipoles $\vec{m}_i, \vec{m}_j$, located at $\vec{r}_i, \vec{r}_j$

$$E_{ms}(i,j) = -\frac{1}{4\mu_0}\frac{3\vec{m}_i \cdot \vec{R}_{ij}\vec{m}_j \cdot \vec{R}_{ij} - \vec{m}_i\vec{m}_j R_{ij}^2}{R_{ij}^5} \tag{2.6}$$

where $\vec{R}_{ij} = \vec{r}_i - \vec{r}_j$. The equation above however only takes into account one pair of dipoles, in reality one has to sum over $\sum_{i>j} E_{ms}(i,j)$ and that becomes very quickly very cumbersome. Therefore we replace the sums with integrals, $\sum_i ..\vec{m}_i = \int ..\vec{M}(\vec{r})dV$ and get

$$E_{ms} = -\frac{1}{2}\mu_0 \int_V \vec{H}_d(\vec{r}) \cdot \vec{M}(\vec{r})dV \tag{2.7}$$

$\vec{H}_d$ is the demagnetization field. Generally the demagnetization field depends on the position within the magnetic material, but for ellipsoids it is constant inside the medium and can be approximated to [10]

$$\vec{H}_d = -\mathbf{N}\vec{M} \tag{2.8}$$

whereby **N** is the demagnetization tensor which will be further discussed later on when we talk about how to calculate the demagnetization energy in micromagnetic modelling. However it has the property $trace(N) = 1$ and has a simple form for the shape of an infinitely long wire, a sphere and an infinite two dimensional plate [10]

$$\mathbf{N}_{sphere} = \begin{bmatrix} \frac{1}{3} & 0 & 0 \\ 0 & \frac{1}{3} & 0 \\ 0 & 0 & \frac{1}{3} \end{bmatrix}, \mathbf{N}_{wire} = \begin{bmatrix} \frac{1}{2} & 0 & 0 \\ 0 & \frac{1}{2} & 0 \\ 0 & 0 & 0 \end{bmatrix}, \mathbf{N}_{plate} = \begin{bmatrix} 0 & 0 & 0 \\ 0 & 0 & 0 \\ 0 & 0 & 1 \end{bmatrix} \tag{2.9}$$

Anisotropy	Mechanism	Uniaxial constant
Crystalline	Crystal field	$k_u = k_1$
Shape	Magnetostatic	$k_u = k_{shape} = \frac{1}{2}\mu_0 M_s^2$
Stress	Magnetoelastic	$k_u = k_{stress} = \frac{3}{2}\lambda_s \sigma$

Table 2.1: Anisotropy constant with different sources which are relevant for the sensors at the heart of this thesis

Using (2.8) and (2.7) we get

$$E_{ms} = \frac{1}{2}\mu_0 \vec{M}\mathbf{N}\vec{M}V \tag{2.10}$$

Magnetic layers can be described by the demagnetization tensor of the infinite plate. In a coordinate system where the z-axis is parallel to the surface normal with $\mathbf{N}_{plate}$ we get

$$E_{ms} = \frac{1}{2}\mu_0 M_S^2 cos^2(\theta) = k_{shape} sin^2(\theta) + const. \tag{2.11}$$

$$k_{shape} = \frac{1}{2}\mu_0 M_S^2 \tag{2.12}$$

This energy is minimized if the magnetization is oriented parallel to the plane.

2.3 Stress induced anisotropy

The interaction between the magnetization and the strains ϵ_{ij} gives rise to a contribution to the elastic energy of a magnetic solid. The magnetoelastic energy E_{me} is the increase in anisotropy energy of a magnetic solid when it is submitted to stress. Its expression for a cubic crystal is given as [11]

$$\begin{aligned}\frac{E_{me}}{V} = \frac{1}{2}c_{11}(\epsilon_{xx}^2 + \epsilon_{yy}^2 + \epsilon_{zz}^2) + \frac{1}{2}c_{44}(\epsilon_{xy}^2 + \epsilon_{yz}^2 + \epsilon_{zx}^2) \\ + c_{12}(\epsilon_{yy}\epsilon_{zz} + \epsilon_{xx}\epsilon_{zz} + \epsilon_{xx}\epsilon_{yy})\end{aligned} \tag{2.13}$$

c_{ij} are the elastic moduli which can be looked up in [11] for iron and nickel. Magnetostriction is the change of the solids dimensions as its magnetic state is changed. It is measured by the relative linear deformation ϵ

$$\epsilon = \frac{\delta l}{l_0} \tag{2.14}$$

Where $\delta l = l - l_0$ is the change in the linear dimension of the solid. The saturation magnetostriction λ_s, which is the magnetistriction corresponding to a solid magnetized to saturation is related to E_{me} for a cubic crystal which is being submitted to a stress σ by

$$\frac{E_{me}}{V} = \frac{3}{2}\lambda_s \sigma sin^2(\theta) \tag{2.15}$$

where θ is the angle between the direction of magnetization and the direction along which the magnetostriction is measured. This yields

$$k_{stress} = \frac{3}{2}\lambda_s \sigma \tag{2.16}$$

2.4 Superposition of anisotropies

If a magnetic system is subject to two uniaxial anisotropies the free energy density is given as

$$e_{ani} = k_a sin^2(\phi_a - \theta) + k_b sin^2(\phi_b - \theta) \tag{2.17}$$

where θ is the angle to an arbitrary reference axis and ϕ_a, ϕ_b are the angle of the easy axis to the same arbitrary reference axis respectively, as shown in figure 2.3.

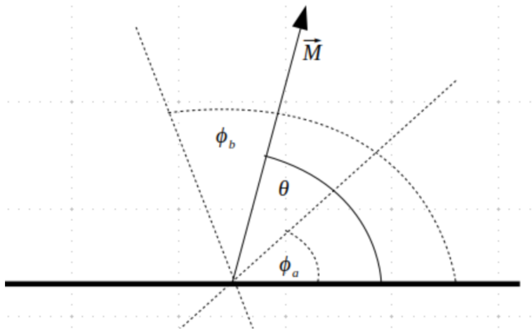

Figure 2.3: Schematic of a magnetization which is superimposed by two uniaxial anisotropies. Both anisotropy axes and the magnetization lie in the same plane.

The simplification which we assume, is that the magnetization lies in the same plane as the anisotropies, this is reasonable for thin films. Generally speaking the resulting anisotropy of two or more uniaxial anisotropies is not uniaxial, however the 2D in plane model is justified if some other anisotropy (e.g. the shape anisotropy) forces the magnetization into the aforementioned plane, therefore we assume that for this following calculation the 2D approximation is applicable and with the identity $sin^2 x = \frac{1-cos2x}{2}$ we can rewrite (2.17) as

$$e_{ani} = \frac{k_a}{2} + \frac{k_b}{2} - \frac{k_a}{2} cos2(\theta - \phi_a) - \frac{k_b}{2} cos2(\theta - \phi_b) \tag{2.18}$$

where the constant terms can be ignored since they don't contribute to the magnetization dynamics. Using sine and cosine sum identities we can further write

$$\begin{aligned} e_{ani} = -\left[\frac{k_a}{2} cos2\phi_a - \frac{k_b}{2} cos2(\theta - \phi_b)\right] cos2\theta - \left[\frac{k_a}{2} sin2\phi_a - \frac{k_b}{2} sin2(\theta - \phi_b)\right] sin2\theta \\ = -\frac{k_c}{2} cos2(\theta - \phi_c) \end{aligned} \tag{2.19}$$

where we have defined the new expressions k_c the effective anisotropy resulting from the two anisotropies and ϕ_c the angle of the new easy axis relative to the aforementioned referance axis. Combining the anisotropies in two single expressions gives

$$\frac{k_c}{2} sin2\phi_c := \frac{k_a}{2} sin2\phi_a + \frac{k_b}{2} sin2\phi_b \tag{2.20}$$

$$\frac{k_c}{2} cos2\phi_c := \frac{k_a}{2} cos2\phi_a + \frac{k_b}{2} cos2\phi_b \tag{2.21}$$

In order to obtain an expression for k_c we evaluate $(\frac{k_c}{2} sin2\phi_c)^2 + (\frac{k_c}{2} cos2\phi_c)^2$ and get

$$k_c = \sqrt{k_a^2 + k_b^2 + 2k_a k_b cos2(\phi_a - \phi_b)} \tag{2.22}$$

where we neglected the negative solution of the square root for k_c. In order to obtain the direction of the easy axis ϕ_c one simply needs to evaluate $\frac{\frac{k_c}{2} sin2\phi_c}{\frac{k_c}{2} cos2\phi_c}$

$$\phi_c = \frac{1}{2} \arctan \frac{k_a sin2\phi_a + k_b sin2\phi_b}{k_a cos2\phi_a + k_b cos2\phi_b} \tag{2.23}$$

where one has to be careful to evaluate the arctangent in the right quadrant, for instruction on how to do that see [28].

2.5 Anisotropy field

A material parameter which will become useful later, when talking about calculating parameters for the simulations is the anisotropy field $\vec{H_K}$. The anisotropy field describes how the crystalline anisotropy effects the magnetization. Lets consider that the magnetization $\vec{m}$ rotates out of the easy axis, the crystaline anisotropy would in that case create a torque which would push $\vec{m}$ back to the easy axis, the anisotropy field, which is supposed to have the same effect as the crystaline anisotropy, is parallel to the easy axis and its magnitude is such that its torque is that of the crystaline anisotropy. As already stated in (2.2) the energy is dependent on the angle θ, then the torque is the derivate of the energy with respect to the angle [9]

$$T = \frac{\partial e}{\partial \theta} \tag{2.24}$$

Using the Zeeman energy, which will be discussed more in depth later down the line, we can write

$$e_K = -\mu_0 M_s H_K cos(\theta) \tag{2.25}$$

The associated torque for small θ is

$$T_k = \mu_0 M_S H_K sin(\theta) \approx \mu_0 M_S H_K \theta \tag{2.26}$$

Inserting the first order term of (2.2) into (2.24) yields

$$T_{ani} = 2k_1 sin(\theta) cos(\theta) = k_1 sin(2\theta) \approx 2k_1\theta \tag{2.27}$$

By definition[42] we know that $T_K = T_{ani}$ which gives

$$H_K = \frac{2k_1}{\mu_0 M_s} \tag{2.28}$$

Lets consider something a little different to get a better understanding of H_K. Applying an external magnetic field $\vec{H}$, wich is perpendicular to the easy axis, will increase θ due to the torque $\vec{H}$ creates. The total torque is set to zero to obtain the equilibrium condition

$$-\mu_0 M_S H cos(\theta) + 2k_1 sin(\theta) cos(\theta) = 0 \tag{2.29}$$

$\vec{M}$ is parallel to the field $\vec{H}$ when $sin(\theta) = 1$, this yields $H = 2k_1/(\mu_0 M_s) = H_K$, which means that saturation is reached when $H = H_K$.

Chapter 3

Micromagnetism

Hysteresis is a characteristic feature of magnets and its prediction is possible utilizing micromagnetism. In micromagnetism the input parameters are the microstructure(geometry) of the magnetic system as well as M_s, k_1, A $\vec{H}_{Zee}$. Hysteresis has been known for quite some time before modern micromagnetics started with a paper by Landau and Lifschitz(1935) who put Blochs ideas onto a physical basis.
Micromagnetism does not account for distinct magnetic spins but integrates quantum mechanical effects that are essential to ferromagnetism,e.g. the exchange interaction, with a classical continuous field description of the magnetization, which means that one moves away from a discrete lattice of atomic spins and adopts a continuous vector density $\vec{M}(\vec{r})$. The main claim this model makes is that the organizing forces within the magnetic material are strong enough to keep the magnetization parallel on a characteristic length scale $\lambda = \sqrt{k_{eff}/A}$, where k_{eff} is the effective anisotropy and A is the exchange constant, which is well above the lattice constant a. Therefore it states

$$\vec{M}_i \approx \vec{M}_j \text{ for } |\vec{r}_i - \vec{r}_j| = a \ll \lambda \tag{3.1}$$

$\vec{M}_i$ and $\vec{M}_j$ are the magnetization at positions $\vec{r}_i$ and $\vec{r}_j$ respectively. Additionally one assumes a homogeneous density of spins which means that the magnetization $\vec{M}(\vec{r})$ has a constant norm $|\vec{M}(\vec{r})| = M_s$ and therefore can be written as a unit vector field $\vec{m}(\vec{r})$

$$\vec{M}(\vec{r}) = M_s\vec{m}(\vec{r}) \;\; |\vec{m}(\vec{r})| = 1 \tag{3.2}$$

In the case of zero temperature, which will always be the case in the results of this work and is often considered for micromagnetic modelling M_s is the saturation magnetization, which is a material constant. Micromagnetics is often referred to as a semiclassical theory due to its implementation of quantummechanical effects.

The fact that micromagnetism can predict hysteresis, magnetic switching processes and domain-wall movement makes it perfect for the framework of the software with which the target of this work is supposed to be reached.

3.1 Energy contributions

The total Gibbs-free energy of a ferromagnetic system is given by a number of energy-contributions depending on the properties of the respective magnetic material.As already stated micromagnaetics is composed in part of quantummechanics, therefore some of the contributions are of quantummechanical origin.

3.1.1 Zeeman enegy

As already stated, magnetized bodies are characterized by their magnetic moments $\vec{m}_d = \vec{M}V$, this $\vec{m}_d$ is not to be confused with the normalized magnetization $\vec{m}$. $\vec{m}_d$ is most easily probed by putting the dipole moments in an external magnetic field $\vec{H}$, let us mention that here $\vec{m}$ is not the normalized magnetization but the magnetic moment. The interaction between $\vec{m}$ and $\vec{H}$ is given by:

$$E_{Zee} = -\mu_0 \vec{m}_d \cdot \vec{H} \tag{3.3}$$

This energy contribution is often referred to as Zeeman energy.

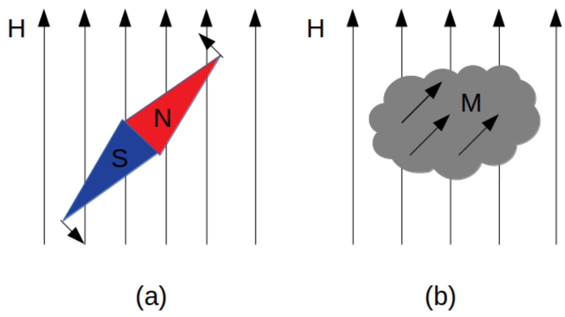

Figure 3.1: Magnetized bodies in a homogenous field: (a) a compass needle and (b) a magnetized body

Figure 3.1(a) shows a very simple example. A compass needle is being subjected to an external magnetic field,its Zeeman-Energy is given by $E_{Zee} = -\mu_0 H m cos(\theta)$, where θ is the angle between the applied field and the magnetic-dipole moment. The lowest energy is obviously obtained for $\theta = 2\pi n$ or $\vec{m}||\vec{H}$. Meaning that E_{Zee} is minimal for a compass needle pointing parallel to the applied magnetic field.
As already stated micromagnetics does not deal with single magnetic-dipole moments but has a continuous magnetization across the ferromagnetic body(Figure 3.1(b)), which means one needs to upgrade (3.3) to fit the continuous medium:

$$E_{Zee} = -\mu_0 \int_{\Omega_m} M_s \vec{m}(\vec{r}) \cdot \vec{H}(\vec{r}) d\vec{r} \tag{3.4}$$

Here $\vec{m}$ is the normalized magnetization. The above equation yields the Zeeman energy of a magnetic body Ω_m.

3.1.2 Demagnetization Energy

The demagnetization energy accounts for the dipole-dipole interaction within a magnetic system. Its name derives from the fact that magnetic systems energetically favor demagnetized states if dipole-dipole interaction is the only thing they are subjected to, it is also referred to as magnetostatic energy or stray-field energy.
The demagnetization energy can be derived using Maxwells Equations for a vanishing electric current $\vec{j}_e = 0$:

$$\nabla \cdot \vec{B} = 0, \;\; \nabla \times \vec{H}_{dem} = 0 \tag{3.5}$$

The magnetic flux $\vec{B}$ can than be written in terms of $\vec{H}_{dem}$ and $\vec{M}$ as:

$$\vec{B} = \mu_0 (\vec{H}_{dem} + \vec{M}) \tag{3.6}$$

The demagnitizing field $\vec{H}_{dem}$ is conservative due to (3.5), which means that $\vec{H}_{dem}$ has a scalar potential $u(\vec{r})$, $\vec{H}_{dem} = -\nabla u$ and that (3.5) can be reduced to:

$$\nabla \cdot (-\nabla u + \vec{M}) = 0 \tag{3.7}$$

Assuming the magnetization is localized in a finite region, the boundary conditions for the potential $u(\vec{r})$ are given in an asymptotical fashion by:

$$u(\vec{r}) = \mathcal{O}(1/|\vec{r}|) \text{ for } |\vec{r}| \to \infty \tag{3.8}$$

This is referred to as open boundary condition since the potential is supposed to nullify at infinity. Equation (3.7) is another form of Poisson's equation

$$\Delta u = \nabla \cdot \vec{M} \tag{3.9}$$

Meaning that one can express this potential $u(\vec{r})$ in terms of an integral equation using the fundamental solution of the Laplacian that obviously meets the required open boundary condition [3].

$$u(\vec{r}) = -\frac{1}{4\pi} \int \frac{\nabla' \cdot \vec{M}(\vec{r'})}{|\vec{r} - \vec{r'}|} d\vec{r'} \tag{3.10}$$

This solution, same as (3.9), suffers from the problem that $\vec{M}(\vec{r})$ is localized and therefore $\vec{M}(\vec{r})$ jumps suddenly from M_s to zero. This sudden jump means that the divergence in (3.9) & (3.10) is singular at the boundary of the magnetic body.

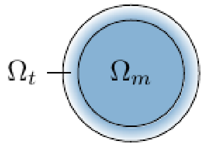

$$|\boldsymbol{M}(\boldsymbol{x})| = \begin{cases} M_s & \text{for } \boldsymbol{x} \in \Omega_m \\ < M_s & \text{for } \boldsymbol{x} \in \Omega_t \\ 0 & \text{otherwise} \end{cases}$$

Figure 3.2: Magnetization $\vec{M}$ is defined within the magnetic region Ω_m and continuously decreases in shell region Ω_t. Figure taken from [3].

This problem is rectified by considering a finite magnet with $|\vec{M}(\vec{r})| = M_s$ for $\vec{r} \in \Omega_m$, which is surrounded by a thin shell Ω_t where the magnetization decays continuously to zero, this is shown in Fig. 3.3. Having done that, one can reduce (3.10) to an integration over $\Omega_m \cup \Omega_t$, furthermore the integral over Ω_t is transformed with Green's theorem

$$\int_{\Omega_t} \frac{\nabla' \cdot \vec{M}(\vec{r'})}{|\vec{r} - \vec{r'}|} d\vec{r'} = \int_{\partial\Omega_t} \frac{\vec{M}(\vec{r'}) \cdot \vec{n}}{|\vec{r} - \vec{r'}|} d\vec{s'} - \int_{\Omega_t} \vec{M}(\vec{r'}) \cdot \nabla' \frac{1}{|\vec{r} - \vec{r'}|} d\vec{r'} \tag{3.11}$$

where $d\vec{s'}$ denotes the areal measure to $\vec{x'}$ and $\vec{n}$ is an outward pointing normal vector. To mimic a real magnet one has to consider the limit for a vanishing transition region $\Omega_t \Rightarrow 0$. This means that the right hand side of 3.11 reduces to the boundary integral and since the magnetization vanishes at the outer boundary the boundary integral vanishes too for the outer boundary of Ω_t. However the inner boundary of Ω_t coincides with the outer boundary of the region $\partial\Omega_m$ except for its orientation. Therefore the integral form of the magnetic scalar potential of an ideal localized magnet in region Ω_m reads as follows:

$$u(\vec{r}) = -\frac{1}{4\pi} [\int_{\Omega_m} \frac{\nabla' \vec{M}(\vec{r'})}{|\vec{r} - \vec{r'}|} d\vec{r'} - \int_{\partial\Omega_m} \frac{\vec{M}(\vec{r'}) \cdot \vec{n}}{|\vec{r} - \vec{r'}|} d\vec{s'}] \tag{3.12}$$

Applying Green's theorem to (3.12) yields:

$$u(\vec{r}) = \frac{1}{4\pi} \int_{\Omega_m} \vec{M}(\vec{r'}) \cdot \nabla' \frac{1}{|\vec{r} - \vec{r'}|} d\vec{r'} \tag{3.13}$$

The demagnetization field $\vec{H}_{dem}$ can then be expressed as a convolution:

$$\begin{aligned}\vec{H}_{dem}(\vec{r}) &= -\nabla u(\vec{r}) = -\frac{1}{4\pi}\int_{\Omega_m} \vec{M}(\vec{r}')\cdot\nabla\nabla'\frac{1}{|\vec{r}-\vec{r}'|}d\vec{r}' \\ &= \int_{\Omega_m} \vec{M}(\vec{r}')\tilde{N}(\vec{r}-\vec{r}')d\vec{r}' = (\vec{M}*\tilde{N})(\vec{r})\end{aligned} \tag{3.14}$$

with the so called demagnetization tensor $\tilde{N}$ given by:

$$\tilde{N}(\vec{r}-\vec{r}') = -\frac{1}{4\pi}\nabla\nabla'\frac{1}{|\vec{r}-\vec{r}'|} \tag{3.15}$$

The energy contribution by the demagnetization energy is then given by:

$$E_{dem} = -\frac{\mu_0}{2}\int_{\Omega_t} \vec{M}\cdot\vec{H}_{dem}d\vec{r} \tag{3.16}$$

The factor 1/2 accounts for the quadratic dependence of the energy on the magnetization $\vec{M}$.

3.1.3 Exchange energy

The exchange interaction is responsible for establishing magnetic order in magnetic materials, this interaction has no classic analogue and arises from quantum mechanics.

In ferromagnetics two localized spins favor a parallel over an antiparallel spin, this originates in the Coulomb energy of the two-electron system. The exchange between two individual spins $\vec{S}_i, \vec{S}_j$ can be described by the hamiltonian [5]

$$\mathcal{H} = -2J\vec{S}_i\cdot\vec{S}_j \tag{3.17}$$

where J is the exchange integral, which is a measure for the intensity of the interaction. (3.17) is widely known as the Heisenberg model and is used for the description of many magnetic properties. The interaction energy can than be written as

$$E_{ij}^{ex} = -2JS^2\vec{m}_i\cdot\vec{m}_j \tag{3.18}$$

where we used the reduced magnetization $\vec{m} = \frac{\vec{M}}{M_s}$ with M_s for saturation magnetization. When considering a continuous magnetization $\vec{m}(\vec{r})$, the exchange energy associated with all pairings of a single spin site at $\vec{r}$ is given by

$$\begin{aligned}E_{ex} &= \sum_i J_i\vec{m}(\vec{r})\cdot\vec{m}(\vec{r}+\Delta\vec{r}_i) \\ &= \sum_i J_i[1-\frac{1}{2}(\nabla\vec{m}^T\cdot\Delta\vec{r}_i)^2] + \mathcal{O}(\Delta x_i^3)\end{aligned} \tag{3.19}$$

where the index i runs over all coupled spin sites $\vec{r}_i$, and J_i denotes the exchange integral between the respective spins. (3.19) is obtained by application of the unit-vector identity $(\vec{n}_1-\vec{n}_2)^2 = 2-2\vec{n}_1\cdot\vec{n}_2$ and performing a Taylor expansion of lowest order. To transition from the discrete Heisenberg model to a continuous expression for E_{ex} one integrates (3.19), while considering regular spacing of spin sites $\vec{r}_i$ and identical J_i and $\Delta\vec{r}_i$ for each site. The most general form yields:

$$E_{ex} = C + \int_{\Omega_m}\sum_{i,j,k} A_{jk}\frac{\partial m_i}{\partial r_j}\frac{\partial m_i}{\partial r_k}d\vec{r} \tag{3.20}$$

where the tensor A_{jk} is denoted as the exchange tensor. The exchange tensor is deeply connected to the exchange integral[5] and yields the strength of the magnetic coupling and therefore measures how difficult it is for a given spin to deviate from the direction of the exchange field. The term C results from the integration of the constant part of (3.19) and will be neglected in the next step since it doesn't depend on $\vec{m}$ and therefore doesn't change the physics of the system. With a proper choice of coordinate system the exchange tensor A_{jk} can be diagonalized [6]

$$E_{ex} = \int_{\Omega_m} \sum_{i,j} A_j (\frac{\partial m_i}{\partial r'_j})^2 d\vec{r}' \tag{3.21}$$

The exchange tensor A_{jk} can even further be simplified for cubic and isotropic lattice structures to the exchange constant A[5]

$$E_{ex} = \int_{\Omega_m} A \sum_{i,j} (\frac{\partial m_i}{\partial r_j})^2 d\vec{r} = \int_{\Omega_m} A (\nabla \vec{m})^2 d\vec{r} \tag{3.22}$$

Crystalline anisotropy energy

As already stated the anisotropy energy favors the magnetization to be parallelly aligned to certain axes, which are referred to as easy axes. This topic has already been sufficiently explored in previous chapters, so let's just for the sake of completion mention the most important properties of the anisotropy energy, which are the following.

The easy axes are undirected for a unidirectional magnet and therefore the energy does not depend on the sign of the magnetization

$$E_{ani}(\vec{m}) = E_{ani}(-\vec{m}) \tag{3.23}$$

The anisotropy energy for a single easy axis is given by

$$E_{ani} = -\int_{\Omega_m} [k_1 sin^2\theta + k_2 sin^4\theta + ...] d\vec{r} \tag{3.24}$$

3.1.4 Other contributions

There are various other effects that may play vital roles in describing the magnetic system in question.

For example the spins can be subjected to an antisymetric exchange interaction in addition to the regular exchange interaction which was discussed before. This was discovered by Dzyloshinskii [14] and Moriya [15] and is relevant for magnetic layers which have an interface to a heavy metal layer. Another contribution that might be interesting if one where to expand the scope of this thesis is the interlayer exchange energy, which was discovered by Rudermann and Kittel [11]. The interlayer exchange energy gives rise to the idea that magnetic layers of a multilayer structure are coupled even if they are separated by a nonmagnetic spacer layer.

However for this work only the above discussed contributions will be of relevance.

3.2 Static micromagnetism

In order to investigate the hysteresis of different magnetic devices one has to have a theory of stable magnetization, enter static micromagnetics. In order for a magnetization to be stable it needs to minimize the total free energy E of the system with respect to $\vec{m}$, in addition to fulfilling the condition (3.2), therefore

$$\min E(\vec{m}) \text{ subject to } |\vec{m}(\vec{r})| = 1 \tag{3.25}$$

Since the solution $\vec{m}$ is a continuous vector field, variational calculus has to be applied in order to solve for an energetic minimum. The condition brought forth is a functional differential that vanishes for an arbitrary test function $\vec{v} \in V_m$ where V_m is the function space of $\vec{m}$

$$\delta E(\vec{m}, \vec{v}) = \frac{d}{d\epsilon} E(\vec{m} + e\vec{v}) = \lim_{\epsilon \to 0} \frac{E(\vec{m} + \epsilon\vec{v} - E(\vec{m}))}{\epsilon} = 0 \ \forall \ \vec{v} \in V_m \tag{3.26}$$

Alternatively one could formulate this condition considering the functional derivative $\delta E / \delta \vec{m}$, which is defined as

$$\int_{\Omega_m} \frac{\delta E}{\delta \vec{m}} \cdot \vec{v} \, d\vec{r} = \delta E(\vec{m}, \vec{v}) \ \forall \ \vec{v} \in V_m^0 \tag{3.27}$$

where the function space $V_m^0 \subset V_m$ includes function within V_m that vanish on the boundary $\vec{v}(\partial\Omega_m) = 0$. However depending on the energy E, the differential δE as defined in (3.26) is generally different than (3.27) by a boundary integral

$$\delta E(\vec{m}, \vec{v}) = \int_{\Omega_m} \frac{\partial E}{\partial \vec{m}} \cdot \vec{v} \, d\vec{r} + \int_{\partial\Omega_m} \vec{B}(\vec{m}) \cdot \vec{v} \, d\vec{s} \ \ \forall \ \vec{v} \in V_m \tag{3.28}$$

This means that in order to solve the minimization problem, boundary conditions which are set by $\vec{B}(\vec{m})$ have to be take into account. Up until now, no effort has been made to include the condition $|\vec{m}| = 1$ into our variational considerations. This is incorporated by applying Lagrange multipliers, the derivation can be looked up in [3] it yields Brown's condition

$$\vec{m} \times \frac{\partial E}{\partial \vec{m}} = 0 \tag{3.29}$$

and additionally gives the boundary condition

$$\vec{m} \times \vec{B}(\vec{m}) = 0 \tag{3.30}$$

Zeeman energy

We obtain the energy differential for the Zeeman energy by variation of (3.4)

$$\delta E_{Zee}(\vec{m}, \vec{v}) = \frac{d}{d\epsilon} \left[-\mu_0 \int_{\Omega_m} M_s(\vec{m} + e\vec{v}_m) \cdot \vec{H} \right] \tag{3.31}$$

$$= -\int_{\Omega_m} \mu_0 M_s \vec{H} \tag{3.32}$$

This variation does not give rise to an additional boundary integral. Hence, the derivative and boundary term $\vec{B}$ for the Zeeman energy are given by

$$\frac{\partial E_{Zee}}{\partial \vec{m}} = -\mu_0 M_s \vec{H}, \quad \vec{B} = 0 \tag{3.33}$$

Demagnetization energy

The differential for the demagnetisation energy is obtained similarly to the differential of the Zeeman energy. The only difference is that the demagnetization field $\vec{H}_{dem}(\vec{M})$ depends linearly on the magnetization $\vec{m}$, which yields a factor 2

$$\delta E_{dem}(\vec{m}), \vec{v}) = \frac{d}{d\epsilon}\Big[-\frac{\mu_0}{2}\int_{\Omega_m} M_s(\vec{m}+\epsilon\vec{v}_m)\cdot\vec{H}_{dem}(\vec{m}+\epsilon\vec{v}_m)d\vec{r}\Big]_{\epsilon=0} \tag{3.34}$$

$$= -\int_{\Omega_m} \mu_0 M_s \vec{H}_{dem}\cdot\vec{v}_m d\vec{r} \tag{3.35}$$

The derivative and boundary term are the exact same as (3.33).

Exchange energy

The differential is derived from (3.22)

$$\delta E_{ex}(\vec{m},\vec{v}_m) = \frac{d}{d\epsilon}\Big[\int_{\Omega_m} A[\nabla(\vec{m}+\epsilon\,\vec{v}_m)]^2 d\vec{r}\Big]_{\epsilon=0} \tag{3.36}$$

$$= 2\int_{\Omega_m} a\nabla\vec{m}\cdot\nabla\vec{v}_m d\vec{r} \tag{3.37}$$

In order to avoid spatial derivatives the next step is to integrate by parts

$$\delta E_{ex} = -2\int_{\Omega_m}[\nabla\cdot(A\nabla\vec{m})]\cdot\vec{v}_m\, d\vec{r} + 2\int_{\partial\Omega_m} A\frac{\partial\vec{m}}{\partial\vec{n}}\cdot\vec{v}_m\, d\vec{s} \tag{3.38}$$

This latest expression is of the same form as (3.28), which makes it easy to identify $\delta E_{ex}/\delta\vec{m}$, this also gives rise to a surface integral and thus to a boundary term $\vec{B}$.

$$\frac{\delta E_{ex}}{\delta\vec{m}} = -2\,\nabla\cdot(A\nabla\vec{m}) = -2A\Delta\vec{m} \tag{3.39}$$

$$\vec{B} = 2A\frac{\partial\vec{m}}{\partial\vec{n}} = 0 \tag{3.40}$$

Anisotropy energy

For the uniaxial anisotropy (3.33) the derivative and boundary terms for the first order anisotropy are

$$\frac{\delta E_{ani}}{\delta\vec{m}} = -2k_1\vec{e}_u(\vec{e}_u\cdot\vec{m})\ \ \vec{B} = 0 \tag{3.41}$$

Energy minimization with multiple contribution

In order to minimize the total energy of a system subject to multiple energy contributions the added energy functional needs to fulfill Browns condition (3.29) and the boundary condition (3.30). Lets consider a system which is subject to the exchange-, demagnetization-, crystaline anisotropy- and zeeman energy, we get

$$\vec{m}\times\frac{\delta E}{\delta\vec{m}} = \vec{m}\times(-2A\Delta\vec{m} - \mu_0 M_s\vec{H}_{Dem} - \mu_0 M_s\vec{H}_{Zee} - 2k_1\vec{e}_u(\vec{e}_u\times\vec{m})) = 0 \tag{3.42}$$

$$\vec{B} = 2A\frac{\partial\vec{m}}{\partial\vec{n}} = 0 \tag{3.43}$$

3.3 Discretization with finite differences

Micromagnetism yields a set of nonlinear partial differential equations, which can be solved analytically only for edge cases. Generally the solution of static micromagnetics calls for numerical methods, of which there are plenty. In most cases a discretization for space and if necessary time is introduced, the most popular methods are the finite-difference method (FDM)and the finite-element method(FEM), where the magnetic region is subdivided into individual cells. The difference is that the finite difference method usually requires a regular cuboid mesh while the finite-element method works with irregular tetrahedral mashes. The method has to be carefully chosen dependent on what problem is studied, which is why it was chosen for the simulation of the sensors at the heart of this work. The finite difference method allows the application of very fast algorithms if the restrictions for simple geometries is met. The cell size should be chosen significantly small, so that the structure of the domain walls can be properly resolved. The characteristic length for the domain wall width is the so called exchange length

$$\lambda = \sqrt{\frac{A}{k_{eff}}} \tag{3.44}$$

Finite differences in micromagnetics

k_{eff} is the effective anisotropy constant which includes contributions from the crystalline anisotropy as well as the shape anisotropy, which originates in the demagnetizing field.

Demagnetizing field

The demagnetizing field introduced in previous chapters holds a very special place among the energy contributions, because it is the only long-range interaction. Long-range interactions are computationally expensive, therefore the choice of which spatial discretization to use is significantly influenced by its demagnetizing-field algorithm.

The finite difference method solves partial differential equations by approximating the differential operators with finite-differences. The demagnetization-field(3.9) problem has the form of a Poisson equation, meaning that one would have to approximate the Laplacian operator. However this problem is complicated by the boundary condition(3.8), which prevents the restriction of the computational domain to the magnetic region Ω_m. Therefore the demagnetizing field is solved by direct integration of (3.14).

We consider a cellwise constant normalized magnetization

$$\vec{m}(\vec{r}) = \vec{m}_i \quad \forall \quad \vec{r} \in \Omega_i, \quad \Omega_m = \cup_i \Omega_i \tag{3.45}$$

Inserting this discretization into the integral formulation(3.9) and then averaging over each cell Ω_i gives

$$\vec{H}_i^{dem} = M_s \sum_j \left[\frac{1}{V_c} \int_{\Omega_i} \int_{\Omega_j} \tilde{N}(\vec{r} - \vec{r}') d\vec{r} d\vec{r}' \right] \vec{m}_j = \sum_j A_{ij} m_j \tag{3.46}$$

here V_c is the volume of the mesh cell and A_{ij} denotes the linear demagnetization field operator and not as before the exchange operator. A_{ij} is a dense $3n \times 3n$ matrix with n as the number of simulation cells, meaning that this method scales with $\mathcal{O}(n^2)$. The scaling can be improved by exploiting the convolutional structure of (3.9). In order to preserve this structure we have to restrict our discretization to be regular, meaning all mesh cells have the same shape Ω_{ref}. The offset from one simulation cell $\vec{r}_i$ to another $\vec{r}_j$ is given by

$$\vec{r}_i - \vec{r}_j = \sum_k (i_k - j_k) \Delta r_k \tag{3.47}$$

where Δr_k is the cell spacing in dimension k and $\vec{r}_i, \vec{r}_j$ indicate the positions of two arbitrary simulation cells, using this we get

$$H_i^{dem} = M_s \sum_j \left[\frac{1}{V_i} \iint_{\Omega_{ref}} \tilde{N} \left(\sum_k (i_k - i_j)\Delta r_k + \vec{r} - \vec{r}' \right) d\vec{r} d\vec{r}' \right] m_j = M_s \sum_j \tilde{N}_{i-j} m_j \quad (3.48)$$

$$\tilde{N}_{ij} = \frac{1}{V_i} \iint_{\Omega_{ref}} \tilde{N} \left(\sum_k (i_k - i_j)\Delta r_k + \vec{r} - \vec{r}' \right) d\vec{r} d\vec{r}' \quad (3.49)$$

The discrete demagnetization tensor $\tilde{N}_{i-j}$ has $\Pi_k(2n_k - 1) \approx 8n$ entries, with n_k being the number of cells in spatial dimension k, therefore the storage requirements have been reduced from $\mathcal{O}(n^2)$ to $\mathcal{O}(n)$.

However the computational complexity still remains to be $\mathcal{O}(n^2)$. To reduce it the discrete convolution is done in Fourier space where it reduces to a cellwise multiplication due to

$$\mathcal{F}(\tilde{N} * \vec{m}) = \mathcal{F}(\tilde{N}) \cdot \mathcal{F}(\vec{m}) \quad (3.50)$$

The overall complexity of the demagnetization-field computation is given by the complexity of the fouriertransform-computation, if fast-fouriertransform(FFT) is implemented this amounts to $\mathcal{O}(nlogn)$. However the FFT requires the demagnetization tensor $\tilde{N}_{i-j}$ to be of the same size as the discrete magnetization m_i to perform cell-wise multiplication,this is obviously not the case since m_i has $\Pi_i n_i$ cells and the demagnetization tensor has a size of $\Pi_i\ 2n_i - 1$. This means that the size of the discrete magnetization has to be expanded. Another issues is that all entries of $\tilde{N}_{i-j}$ are considered for every field evaluation, i.e. unphysical distances like $\tilde{N}_{-1,-1}$ are being taken into account. This is remedied by adding zero entries to the magnetization, which is referred to as zero padding [31]. The convolution algorithm is visualized in figure 3.3, where $\vec{M}$ and $\tilde{N}_{ij}$ have been reduced to two dimension for the sake of simplicity. The result is of the size $\Pi_i 2n_i - 1$, but physical meaningfulness is only to be found in the first $\Pi_i n_i$ entries, the remaining ones can be neglected. For three dimensional cuboid cells, Newell et al. derived an analytical formula for $\tilde{N}_{i-j}$[32], where $\tilde{N}_{1-1}$ is given as

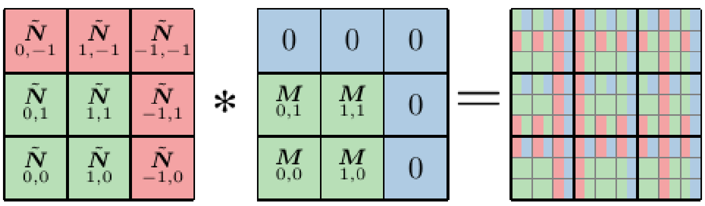

Figure 3.3: Discrete convolution of $\vec{M}$ with $\tilde{N}_{ij}$. The colored blocks represent the convolutions of the respective input values. Figure taken from [3]

$$\begin{aligned} \tilde{N}_{1-1}(\vec{r}, \Delta\vec{r}) = \frac{1}{4\pi \Delta r_1 \Delta r_2 \Delta r_3} \sum_{i,j \in (0,1)} (-1)^{\sum_x i_x + j_x} \\ f[r_1 + (i_1 - j_1)\Delta r_1, r_2 + (i_2 - j_2)\Delta r_2, r_3 + (i_3 - j_3)\Delta r_3] \end{aligned} \quad (3.51)$$

here f is defined as

$$
\begin{aligned}
f(r_1,r_2,r_3) = {} & \frac{|r_2|}{2}(r_3^2 - r_1^2)\sinh^{-1}\left(\frac{|r_2|}{\sqrt{r_1^2+r_2^2}}\right) \\
& + \frac{|r_3|}{2}(r_2^2 - r_1^2)\sinh^{-1}\left(\frac{|r_3|}{\sqrt{r_1^2+r_2^2}}\right) \\
& - |r_1 r_2 r_3|\tan^{-1}\left(\frac{|r_2 r_3|}{r_1\sqrt{r_1^2+r_2^2+r_3^2}}\right) \\
& + \frac{1}{6}(2r_1^2 - r_2^2 - r_3^2)\sqrt{r_1^2+r_2^2+r_3^2}
\end{aligned}
\tag{3.52}
$$

The other diagonal elements $\tilde{N}_{2-2}, \tilde{N}_{3-3}$ can be obtained by circular permutation of the coordinates

$$\tilde{N}_{2-2} = (\vec{r}, \Delta\vec{r}) = \tilde{N}_{1-1}[(r_2, r_3, r_1), (\Delta r_2, \Delta r_3, \Delta r_1)] \tag{3.53}$$

$$\tilde{N}_{3-3} = (\vec{r}, \Delta\vec{r}) = \tilde{N}_{1-1}[(r_3, r_1, r_2), (\Delta r_3, \Delta r_1, \Delta r_2)] \tag{3.54}$$

The off-diagonal element $\tilde{N}_{1,2}$ is given by

$$
\begin{aligned}
\tilde{N}_{1-2}(\vec{r}, \Delta\vec{r}) = {} & \frac{1}{4\pi\Delta r_1 \Delta r_2 \Delta r_3} \sum_{i,j\in(0,1)} (-1)^{\sum_x i_x + j_x} \\
& g[r_1 + (i_1 - j_1)\Delta r_1, r_2 + (i_2 - j_2)\Delta r_2, r_3 + (i_3 - j_3)\Delta r_3]
\end{aligned}
\tag{3.55}
$$

where g is defined as

$$
\begin{aligned}
g(r_1,r_2,r_3) = {} & (r_1 r_2 r_3)\sinh^{-1}\left(\frac{r_3}{\sqrt{r_1^2+r_2^2}}\right) \\
& + \frac{r_2}{6}(3r_3^2 - r_2^2)\sinh^{-1}\left(\frac{r_1}{\sqrt{r_2^2+r_3^2}}\right) \\
& + \frac{r_1}{6}(3r_3^2 - r_1^2)\sinh^{-1}\left(\frac{r_2}{\sqrt{r_2^2+r_3^2}}\right) \\
& - \frac{r_3^3}{6}\tan^{-1}\left(\frac{|r_1 r_2|}{r_3\sqrt{r_1^2+r_2^2+r_3^2}}\right) - \frac{r_3 r_2^2}{6}\tan^{-1}\left(\frac{|r_1 r_3|}{r_2\sqrt{r_1^2+r_2^2+r_3^2}}\right) \\
& - \frac{r_3 r_1^2}{6}\tan^{-1}\left(\frac{|r_2 r_3|}{r_1\sqrt{r_1^2+r_2^2+r_3^2}}\right) - \frac{r_1 r_2\sqrt{r_1^2+r_2^2+r_3^2}}{3}
\end{aligned}
\tag{3.56}
$$

The elements off the diagonal can be obtained similarly as in (3.57,3.58)

$$\tilde{N}_{2-2} = (\vec{r}, \Delta\vec{r}) = \tilde{N}_{1-1}[(r_2, r_3, r_1), (\Delta r_2, \Delta r_3, \Delta r_1)] \tag{3.57}$$

$$\tilde{N}_{3-3} = (\vec{r}, \Delta\vec{r}) = \tilde{N}_{1-1}[(r_3, r_1, r_2), (\Delta r_3, \Delta r_1, \Delta r_2)] \tag{3.58}$$

The discrete tensor $\tilde{N}_{i-j}$ is symmetric therefore the above equations can be used to calculate the remaining elements of the tensor.

Other contributions

The remaining contributions, namely the Zeeman-, Exchange-, and Anisotropy interactions are either short-range or local interactions.

Local contributions to the anistropy energy or the zeeman energy are approximated cellwise

$$H_i^{ani} = \frac{2k_1}{\mu_o M_s}, \quad E_i^{ani} = -\mu_0 M_s \vec{H}_{ani} \cdot \vec{m}_i \tag{3.59}$$

$$E_i^{zee} = -\mu_0 M_s \vec{m}_i \cdot \vec{H} \tag{3.60}$$

here E_i is the energy for the cell respectively.

The exchange field from equation (3.22) is calculated with the approximation of the second derivative in lowest ordered centred finite-differences, which is

$$f''(x) \approx \frac{f(x+\Delta x) - 2f(x) + f(x-\Delta x)}{\Delta x^2} \tag{3.61}$$

The three dimensional Laplacian is then approximated by

$$\Delta \vec{m} \approx \sum_i \frac{\vec{m}(\vec{r} + \Delta r_i \vec{e}_i) - 2\vec{m}(\vec{r}) + \vec{m}(\vec{r} - \Delta r_i \vec{e}_i)}{\Delta r_i^2} \tag{3.62}$$

where the sum goes over the three spatial dimensions i, this results in the discretization of the exchange field $\vec{H}^{ex}$

$$\vec{H}_j^{ex} = \frac{2A}{\mu_0 M_s} \Delta \vec{m}_j \approx \frac{2A}{\mu_0 M_s} \sum_i \frac{\vec{m}(\vec{r}_j + \Delta r_i \vec{e}_i) - 2\vec{m}(\vec{r}_j) + \vec{m}(\vec{r}_j - \Delta r_i \vec{e}_i))}{\Delta r_i^2} \tag{3.63}$$

The boundary condition $\vec{B} = \partial \vec{m}/\partial n = 0$ is implemented by adding virtual cells surrounding the magnetic region Ω_m, as seen in Figure 3.4. At the boundary $x_1 = 0$ this leads to the following equation

$$\left(\frac{\partial m}{\partial x_i}\right)_{(0,j,k)} = \frac{m_{(1,j,k)} - m_{(-1,j,k)}}{2\Delta x_i} = 0 \tag{3.64}$$

which must hold for $0 \leq j \leq n_2 - 1$ and $0 \leq k \leq n_3 - 1$ and
gives $m_{(-1,j,k)} = m_{(1,j,k)}$, this gives all the needed cells for the distinct field computations.

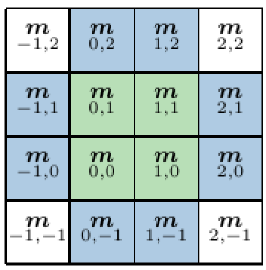

Figure 3.4: The blue squares represent the virtual cells surrounding the magnetic region Ω_m. Figure taken from [3]

3.4 Available software packages

There are various software packages which implement the finite difference method with FFT demagnetization field computation. Some of the most popular are
OOMMFF[33], Fidimag[34] and MicroMagus[35], all of these are running on central processing units(CPUs).

However the recent advent of graphic processing units(GPUs) allowed significant increases in the acceleration of scientific software. A popular open source package is magnum.fd[36], another one which is based on the master thesis of Paul Thomas Heistracher[37] is magnum.af. Throughout this work the latter two will be used.

Chapter 4

Stoner Wolfarth

The first model that was able to describe the magnetism of small particles was developed by Wohlfarth and Stoner in 1948 [12] and is still being used today. This theory treats the magnetic particles as homogeneous single-domain systems with the shape of elongated ellipsoids. To start this of we write the total energy of magnetic system as

$$E = \int_V \left\{ A \left[\nabla \vec{m} \right]^2 + k_1 e_A(\theta) - \frac{\mu_0}{2} \vec{M} \cdot \vec{H}_d(M) - \mu_0 \vec{M} \cdot \vec{H} \right\} dV \tag{4.1}$$

The first term is always zero, since $\nabla \vec{M} = 0$ for a homogenous magnetization. The stoner-wolfarth model therefore corresponds to a simple micromagnetic approach where one neglects the exchange term in the total free energy.

Let us consider a single-domain particle with the shape of an elongated rotationally symmetric ellipsoid, with a homogenous magnetization and easy axis of magnetization along the z direction. If an external magnetic field is added then (4.1) can be transformed to

$$\begin{aligned} \frac{E}{V} &= k_1 sin^2(\theta) + k_2 sin^4(\theta) - \frac{1}{2}\mu_0 N_\perp M_s^2 sin^2\theta \\ -\frac{1}{2}\mu_0 N_\| M_s^2 cos^2\theta &- \mu_0 M_s H \cdot (cos\theta cos\psi + sin\theta sin\psi cos\phi) \end{aligned} \tag{4.2}$$

whereby $N_\perp$ and $N_\|$ are the demagnitizing factors in perpendicular and parallel directions, θ is the angle between the magnetization and the anisotropy axis, ψ is the angle between the external field and the anisotropy axis, these angle are illustrated in Figure 4.1. The physical origin of the anisotropy axis can be the shape- or a sum of crystal- and shape-effects.

If we apply our external magnetic field in z direction, we get $\phi = 0$ and $\psi = 0$, and ignoring second order anisotropy terms it yields

$$\frac{E}{V} = k_1 sin^2\theta - \frac{1}{2}\mu_0 M_s^2 (N_\perp - N_\|) - \mu_0 M_S H cos\theta \tag{4.3}$$

To obtain the angle θ at which the energy is minimized one needs to compute the differential of (4.3)

$$\frac{\partial E(\theta)}{\partial \theta} = 2k_1 sin(\theta)cos(\theta) - \mu_0 M_s^2 sin(\theta)cos(\theta)(N_\perp - N_{||}) - \mu_0 M_s H sin(\theta) = 0 \tag{4.4}$$

To define a minimum we compute the second derivitive, which yields the expression for the coercive field H_C

$$H_C = \frac{2k_1}{\mu_0 M_s} - M_s(N_\perp - N_{||}) \tag{4.5}$$

This result does not depend on the size of the magnet but only on its shape, in the limiting cases of a sphere or a bidimensional plate one gets

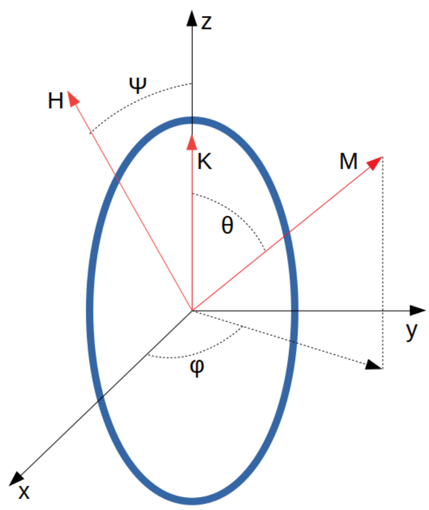

Figure 4.1: Ellipsoidal particle in a magnetic field, showing the relative angles between the external field H, the magnetization M and the anisotropy axis K

$$H_C^{sph} = \frac{2k_1}{\mu_0 M_s} \tag{4.6}$$

and

$$H_C^{pla} = \frac{2k_1}{\mu_0 M_s} + M_s \tag{4.7}$$

The latter of the two expressions will become essential when talking about the parameters of the material we are going to simulate. For $\psi = 0$ (4.4) yields three solutions for the following angles: $\theta = 0$, $\theta = cos^{-1}(\mu_0 M_s H/(2K_1))$, $\theta = \pi$. The first and third solutions correspond to the energy minimum, the second to the maximum. Since $cos(\mu_0 M_s H/(2K_1)) \leq 1$, this expression gives the minimum field which is required to reverse the magnetization

$$H_A = \frac{2k_1}{\mu_0 M_s} \tag{4.8}$$

If we remember the section about the anisotropy field, H_A is the exact same expression as the anisotropy field, which is also the field needed to saturate or invert the magnetization, meaning we arrived at the same result from two different angles.

Knowing the position of the minima one can derive the height of the barrier, corresponding to $\Delta E = E_{max} - E(\theta = 0)$ using algebra

$$\Delta E = k_1 V \left(1 - \frac{H}{H_A}\right)^2 \tag{4.9}$$

which means that the barrier height is proportional to $K_1 V$ and disappears for $H = H_A$. The curves for θ dependent energy $E(\theta)$ for different applied fields are plotted in figure 4.2

In the parallel and perpendicular case for H=0 the energy is minimized if the magnetization points parallel or antiparallel towards the anisotropy, since it is required to obey (2.1). If for the $H \neq 0$ case the field is applied parallelly, the energy is minimized for the direction in which

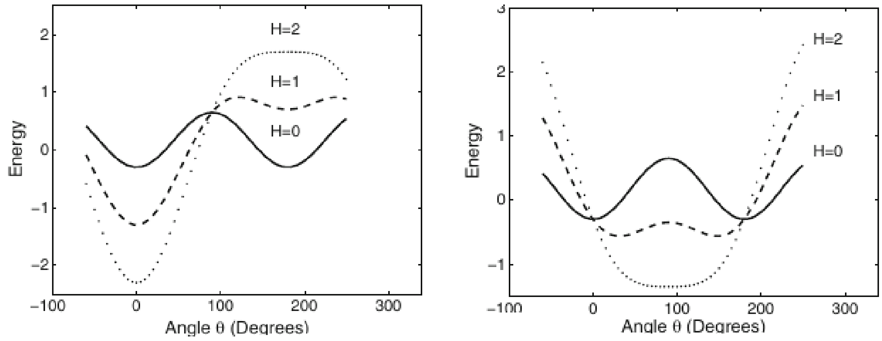

Figure 4.2: Dependence of the energy as a function of the angle between the magnetization and the anisotropy axis $E(\theta)$ in the Stoner-Wolfarth model, for different values of H for (a.) H parallel to the easy axis(i.e. $\psi = 0$) (b.) H perpendicular to the easy axis (i.e. $\psi = \pi/2$) Figure taken from [5]

the magnetic field points, since it basically acts like an additional anisotropy, with the exception that it doesn't obey (2.1). For a sufficiently strong field the minimum will be located along the direction of H, for a weaker field $E(\theta)$ looks essentially similar to the case $H = 0$.

Lets now try to derive hysteresis curves with a stoner wolfarth particle. We are neglecting the magnetostatic term and we look at the first and second derivative to obtain the minima of the energy and the turning point, which corresponds to the point where the magnetization saturates, respectively.

$$E = ksin^2\theta - \mu_0 M_s H_{\|} cos\theta - \mu_0 M_s H_{\perp} sin\theta \tag{4.10}$$

$$\frac{\partial E}{\partial \theta} = 2ksin(\theta)cos(\theta) + \mu_0 M_s H_{\|} sin\theta - \mu_0 M_s H_{\perp} cos\theta = 0 \tag{4.11}$$

$$\frac{\partial^2 E}{\partial \theta^2} = 2k(cos^2\theta - sin^2\theta) + \mu_0 M_s H_{\|}\theta + \mu_0 M_s H_{\perp} sin\theta = 0 \tag{4.12}$$

where we used $H = H_{\|}cos(\phi) + H_{\perp}sin(\phi)$. In order to obtain expressions for the field that is required to saturate the magnetization we look at
$\frac{\partial E}{\partial \theta} sin\theta + \frac{\partial^2 E}{\partial \theta^2} cos\theta$ and $\frac{\partial^2 E}{\partial \theta^2} \sin\theta - \frac{\partial E}{\partial \theta} cos\theta$

$$\frac{\mu_0 M_s}{2K} H_{\|}^* = -cos^3\theta \tag{4.13}$$

$$\frac{\mu_0 M_s}{2K} H_{\perp}^* = sin^3\theta \tag{4.14}$$

$H_{\perp}^*$ and $H_{\|}^*$ are components of the saturation field. These last two equations form the famous Stoner-Wolfarth asteroid, seen in figure 4.3 . The asteroid defines not only the stability limit for equilibrium magnetization direction, but it enables us to determine graphically the possible metastable magnetization directions for any given field $H = H_{\|} + H_{\perp}$ and therefore the hysteresis. The procedure runs as follows: draw a tangent to the astroid from the endpoint of an arbitrary field vector to a tangential point with parameter θ^*. The slope then fulfills the following equation, this is illustrated in figure 4.3

$$\frac{\frac{\mu_0 M_s}{2K} H_{\perp} - sin^3\theta^*}{\frac{\mu_0 M_s}{2K} H_{\|} + cos^3\theta^*} = \frac{\partial H_{\perp}^*/\partial\theta}{\partial H_{\|}^*/\partial\theta} = \frac{\partial sin^3\theta/\partial\theta}{-\partial cos^3(\theta)/\partial\theta} = \frac{3sin^2(\theta)cos(\theta)}{3sin(\theta)cos^2(\theta)} = tan\theta^* \tag{4.15}$$

The first left-hand term is derived by connecting the vector of the applied magnetic field and the point on the stability limit belonging to θ^*, the centre part is simply the slope of the asteroid at this point, which simplifies to $tan(\theta^*)$. However there are more than one possible tangent points for a given field. For the asteroid shown in figure 4.3 we find four tangents if $\vec{h}$ lies inside the asteroid and two otherwise, not all these solutions are stable. In the first case there are two stable solutions while in the second there is only one. The stable solutions are those that have the smaller angle relative to the easy axis. If one were to evaluate these solutions for a series of field values one could derive a complete hysteresis curve for a simple uniaxial particle as shown in figure 4.4.

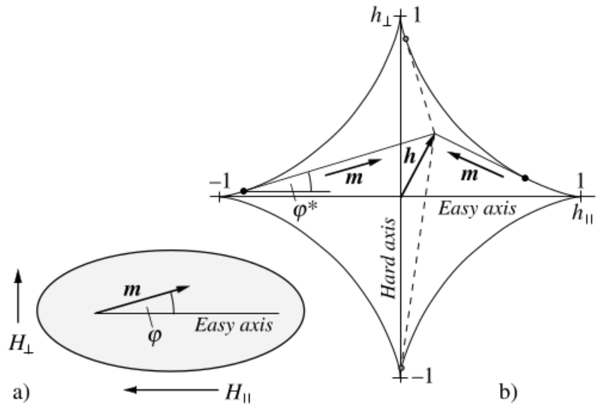

Figure 4.3: The switching curve (b) of an unaixal particle (a) under influence of an external field with the construction of the equilibrium magnetization directions $\vec{m}$. The fields are denoted in reduced units $h = H\mu_0 M_s/2K$. The dashed lines indicate unstable solutions. Figure taken from [13]

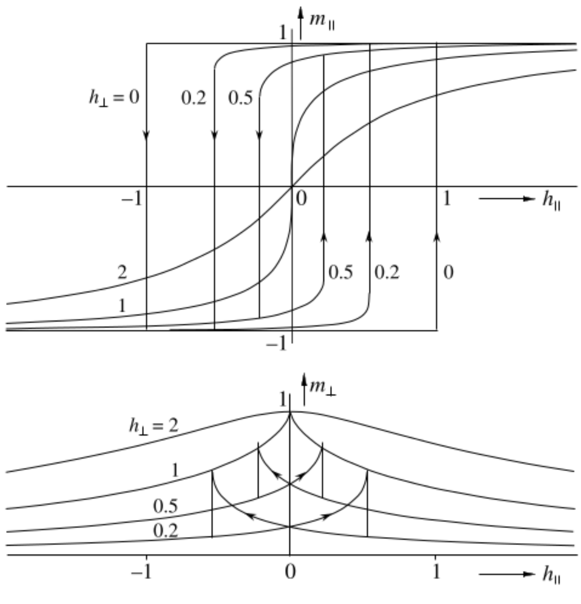

Figure 4.4: Combining the stable solutions which are obtained by Stoner-Wolfarth yields a hysteresis curve of a uniaxial particle. Here longitudinal and transversal magnetization components are shown as a function of the longitudnal field, for different values of the transverse reduced field. Figure taken from [13]

Chapter 5

Simulation of sensors with perpendicular magnetic anisotropy

Before I present the results of this work in full detail, let me first use these opening paragraphs to shortly outline the main results of this chapter.

There are two sensor designs which have been simulated. Firstly there is the out of plane(=OOP) sensor, which is sensitive to in plane magnetic fields and owes its name to the fact that when no magnetic field is applied, the magnetization points out of plane. Secondly there is the in plane(=IP) sensor, which is sensitive to out of plane fields and whose magnetization points in plane, hence the name. A schematic for both is shown in figure 5.1 and the idea behind both of these can be read up on in the following section.

The first simulations which were conducted were of the hysteresis of artificial materials. This means that the individual simulation parameters were taken from preceding publications[28,38,39]. However whether there are actually materials that possess this exact combination of parameters has not been taken care of in this section. This was done in order to understand how the individual parameters affect the hysteresis. Figure 5.2 and figure 5.4 show the variation of the crystal anisotropy constant k and the saturation magnetization M_s respectively for the OOP sensor, where one can see an increase of the slope of the hysteresis for increasing k and a decrease of the slope of the hysteresis for decreasing M_s. The same parameter sweep can be seen for the OOP sensor in figure 5.5 where the hysteresis were affected vice versa to the IP sensor.

The theory of micromagnetism reduces to the stoner-wolfarth model if a magnetic systems exhibits a single domain state. Therefore we used stoner-wolfarth in order to check our results for the single domain state. Stoner-wolfarth equations can be used to calculate the magnetic field at which the magnetization saturates and to determine the hysteresis of a certain magnetic system. Both of these were compared to our simulation for single domain states, which yielded a satisfying overlap, this can be seen in figure 5.6.

Additionally hysteresis which were presented in preceding papers[38,39] have been attempted to reconstruct. Figure 5.7 shows the comparison between experimental[38,29] and simulated data. The overall shape of the hysteresis has been replicated in all cases, however the actual fields where the sensors saturate only overlap in the orders of magnitude but not in the values themselves.

5.1 Sensor configuration

Let us briefly introduce the sensor designs we want to simulate.

Firstly there is the out of plane(=OOP) sensor. The magnitude of the perpendicular crystalline anisotropy k is chosen large enough, so that it overcompensates the shape anisotropy k_{Sh}, meaning the magnetization of the free layer $\vec{m}_{free}$ points out of the plane, when no external field is applied. However k shouldn't be too big because if a magnetic field $\vec{H}$ were to be applied in plane, $\vec{m}_{free}$ should rotate towards the sensor plane until the magnetization is saturated in the y-direction. The pinned layer magnetization $\vec{m}_{pinned}$ is fixed in plane, see figure 5.1(a). All of this means that the sensor is sensitive to in plane magnetic fields $\vec{H}_{IP}$, i.e. this sensor isn't actually sensitive to perpendicular or out of plane fields $\vec{H}_{OOP}$ meaning this is not a z-sensitve sensor but simply an in plane sensor, utilizing perpendicular crystal anisotropy.

Secondly we have the in plane sensor(=IP), which is basically the inverse concept of the OOP sensor.When no field $\vec{H}_{OOP}$ is applied the shape anisotropy k_{Sh} compensates the crystal anisotropy k and $\vec{m}_{free}$ is in plane. If an out of plane field is applied $\vec{H}_{OOP}$ the anistropy energy together with the zeeman energy suffice to tilt the magnetization out of the plane until it is completely perpendicular to the plane, see figure 5.1(b). Hence we get a sensor that is sensitive to $\vec{H}_{OOP}$.

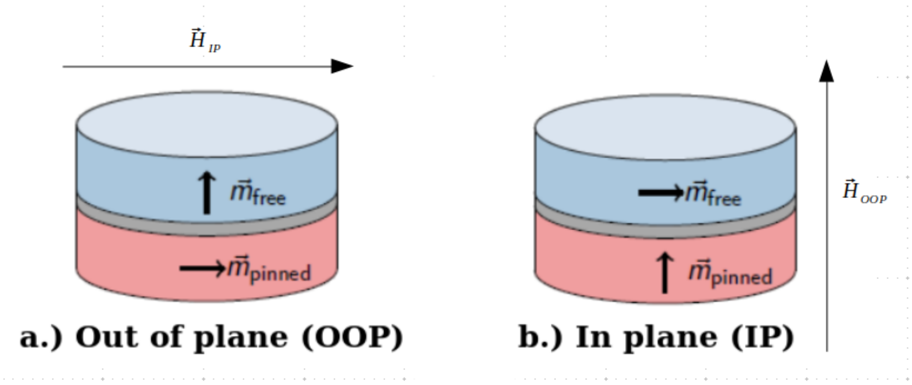

Figure 5.1: Schematics for both sensor designs. a.)The out of plane(=OOP) sensor has a free layer in which the magnetization $\vec{m}_{free}$ points out of plane, while the pinned layer $\vec{m}_{pinned}$ points in plane. b.) The in plane(=IP) sensors magnetization, within the free layer, $\vec{m}_{free}$ points in plane and the pinned magnetization $\vec{m}_{pinned}$ points out of plane.

5.2 Hysteresis with artificial materials

In order to get a feeling for how the individual input parameters change the properties of the magnetic materials as a first step we conduct parameter studies for artificial materials. None of the individual parameters are unphysical, meaning all of them can be found in magnetic materials, but whether there is a specific material that has this exact combination of parameters is neglected, hence artificial materials. However the individual values are not completely made up they are inspired by [28]. The input parameters are unless stated otherwise as shown in table 5.1

Symbol	Description	Value
k	Crystal anisotropy constant	$1.2MJ/m^3$
M_s	Saturation Magnetization	1.75T
A	Exchange constant	$15pJ/m$
h, w, t	height, width, thickness	$6\mu m, 1\mu m, 5nm$
$\vec{m}_{0,IP}$	Initial magnetization for IP	[0,1,0]
$\vec{m}_{0,OOP}$	Initial magnetization for OOP	[0,0,1]

Table 5.1: List of input parameters inspired by [28]

The domainwall width is as already stated given by (3.44), the cell will be chosen accordingly to this since it is essential for the cell to be small enough in order to resolve domain walls.

5.2.1 IP sensor

Parameter study of k

In figure 5.2 hysteresis are shown for the IP sensor as a function of the anisotropy constant as well as certain snapshots from the magnetization configuration, which were made with Paraview. We observe a linear response for small fields, increasing k increases the permeability. This is intuitively clear since the crystal anisotropy points in the z-direction, and the crystal anisotropy gives the direction and the magnitude in which the magnetization energy is minimized. This means that with rising crystal anisotropy constant the field which is needed in order to entirely tilt the magnetization in the z-direction becomes less. Figure 5.2 also illustrates the magnetization configuration for different hysteresis at different points. For crystal anisotropy constants lower than $1.0MJ/m^3$ the hystersis curves are linear, additionally the magnetization configuration does not exhibit any domainwalls, in other words the magnetization is monodomain. But above $1.0MJ/m^3$ the hystereses is not linear anymore, and the domain configuration does not turn smoothly anymore but the monodomain breaks up into something that might be referred to as maze domain structures. To look further into what happens between $k = 1.0MJ/m^3$ and $k = 1.2MJ/m^3$ we further resolve the anisotropy constant and simulate additional anisotropies. It is quite unrealistic to actually resolve these anisotropies in the experiment, but this doesn't matter right now since at the moment we simulate artificial materials. Figure 5.3 shows that the change from uniform magnetization to maze domain structures begins around $1.08MJ/m^3$. Already at zero field a very faint domain structure can be seen, however this domain structure exhibits a hexagonal grid of sorts. It gets much clearer if one increases the crystalline anisotropy constant k to $1.12MJ/m^3$. The domains form a hexagonal grid which can also be found in [43], however if one were to expand the scope of this thesis, further studying this structure and what gives cause to it would be an option.

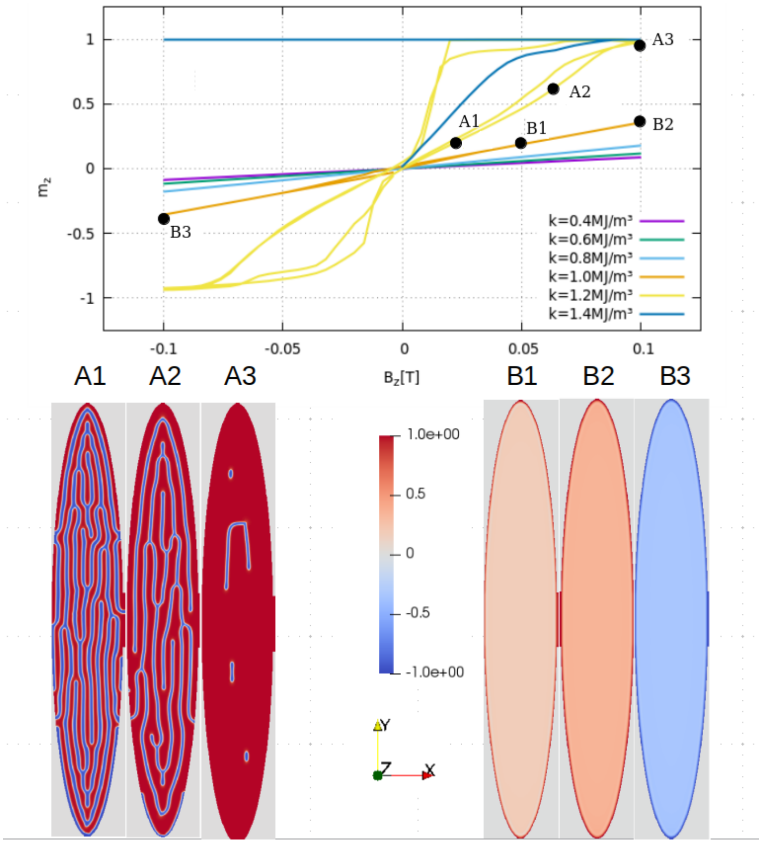

Figure 5.2: Hysteresis of IP sensors as a function of the crystalline anisotropy constant k. Different points within the hysteresis are highlighted, with the matching magnetization configuration below.

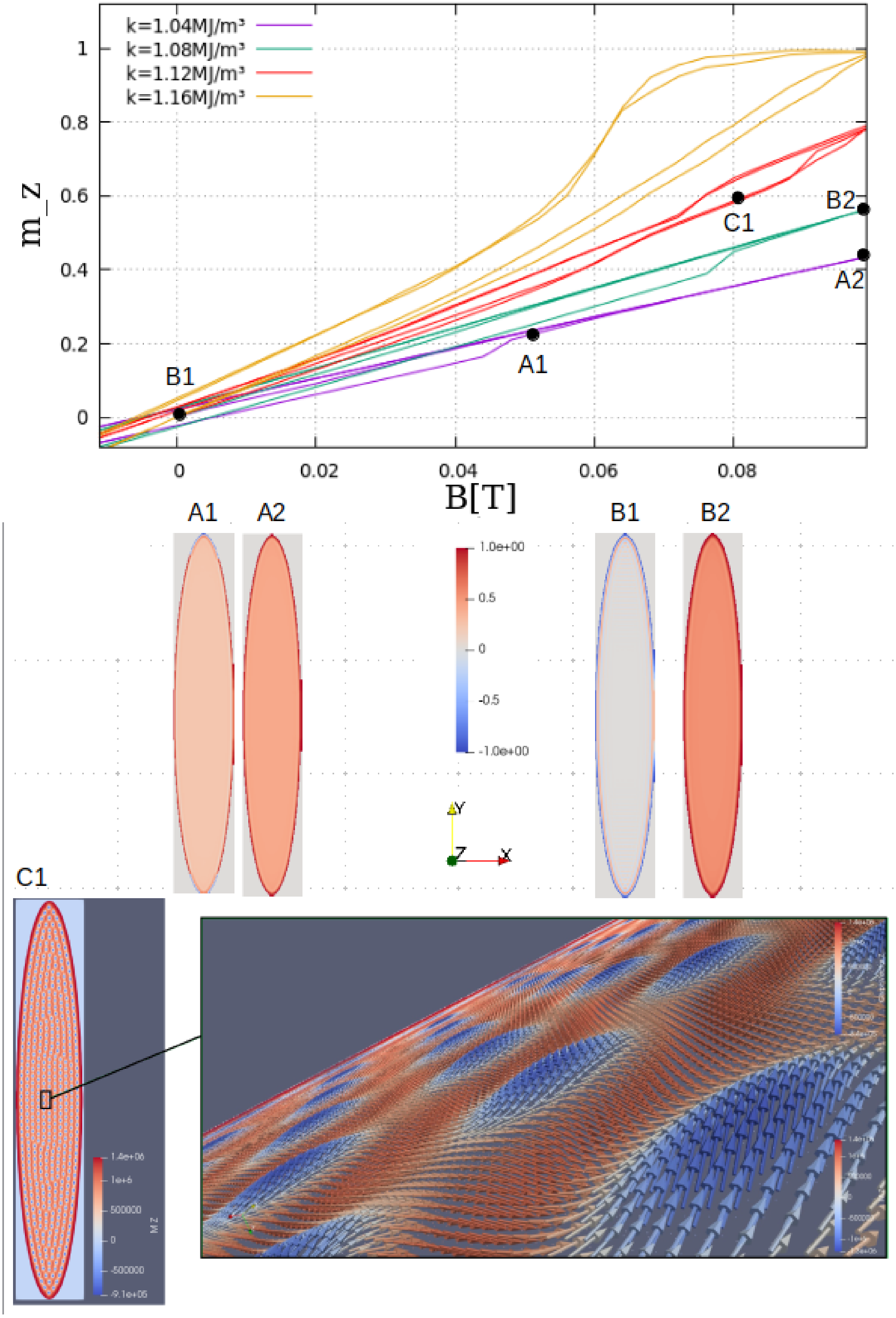

Figure 5.3: The variation in k was resolved more finely in order to examine when the configuration changes from uniform to maze-like. A hexagonal magnetic domain structure is highlighted and zoomed in.

Parameter study of M_s

Next we look at a parameter study of the saturation magnetization M_s. The only interactions which are affected by the saturation magnetization is the demagnetization energy and the Zeeman energy. We have already shown that the demagnetization contribution can be looked at as an anisotropy in the case that the magnetization remains homogeneous. Since we are using magnetic layers this means that, as we showed before, the demagnetization contribution can be looked at as an anisotropy that points along the longest axis of the magnetic layer, which in this case is the y-direction. Meaning that with increasing M_s the shape-anisotropy increases, in other words a bigger field is needed to tilt the magnetization $\vec{m}$ out of the plane if M_s increases, as can be seen in figure 5.4.

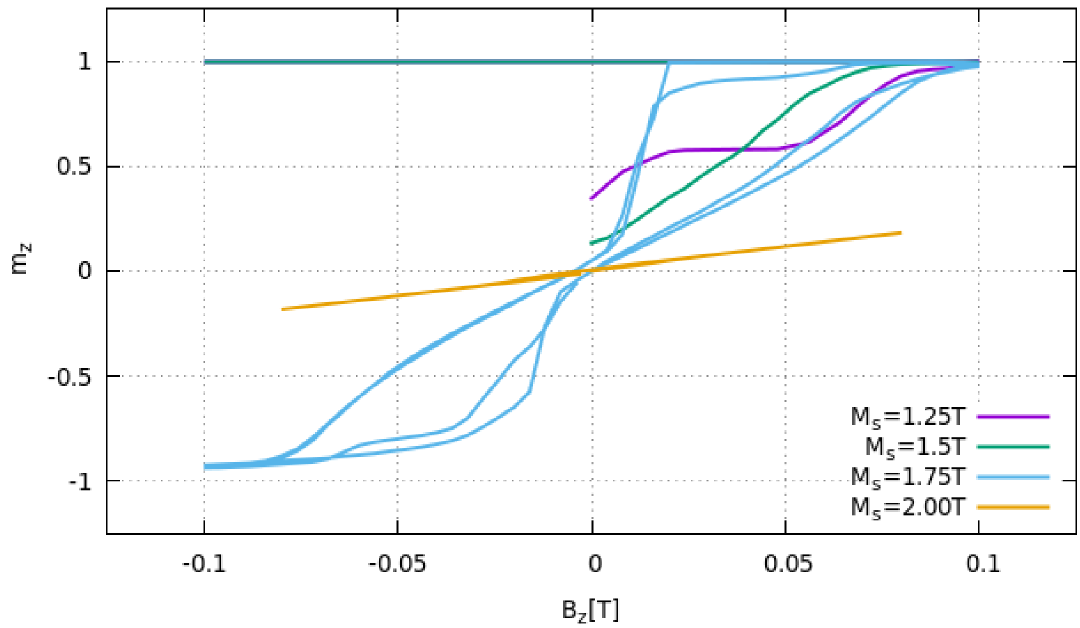

Figure 5.4: Hysteresis of the IP sensor as a function of the saturation magnetization M_s, the parameters that aren't specifically mentioned in the legend were taken from table 5.1

5.2.2 OOP

Parameter study of k & M_s

For the OOP sensors one should note that here all hysteresis curves are in the y-direction, not in the z-direction since the OOP sensors are sensitive to fields which are parallel to y. Since the initial magnetization $\vec{m}$ for the magnetic material is pointing towards the z-direction the anisotropy constant k is significantly larger than before in order to compensate the shape anisotropy entirely and let $\vec{m}$ point out of the plane. Increasing k would mean that it is even more strongly bound to the z-direction, which means that in order to fully tilt this magnetization in the y-direction, the bigger the anisotropy constant the bigger a field is needed to saturate $\vec{m}$, see figure 5.5(a). In contrast the variation of the saturation magnetization M_s, which is directly linked to the demagnetization energy acts as an anisotropy in the y-direction, which increases the permeability if M_s is increased, see figure 5.5(b). In other words M_s takes the same role that k does in the IP sensor.

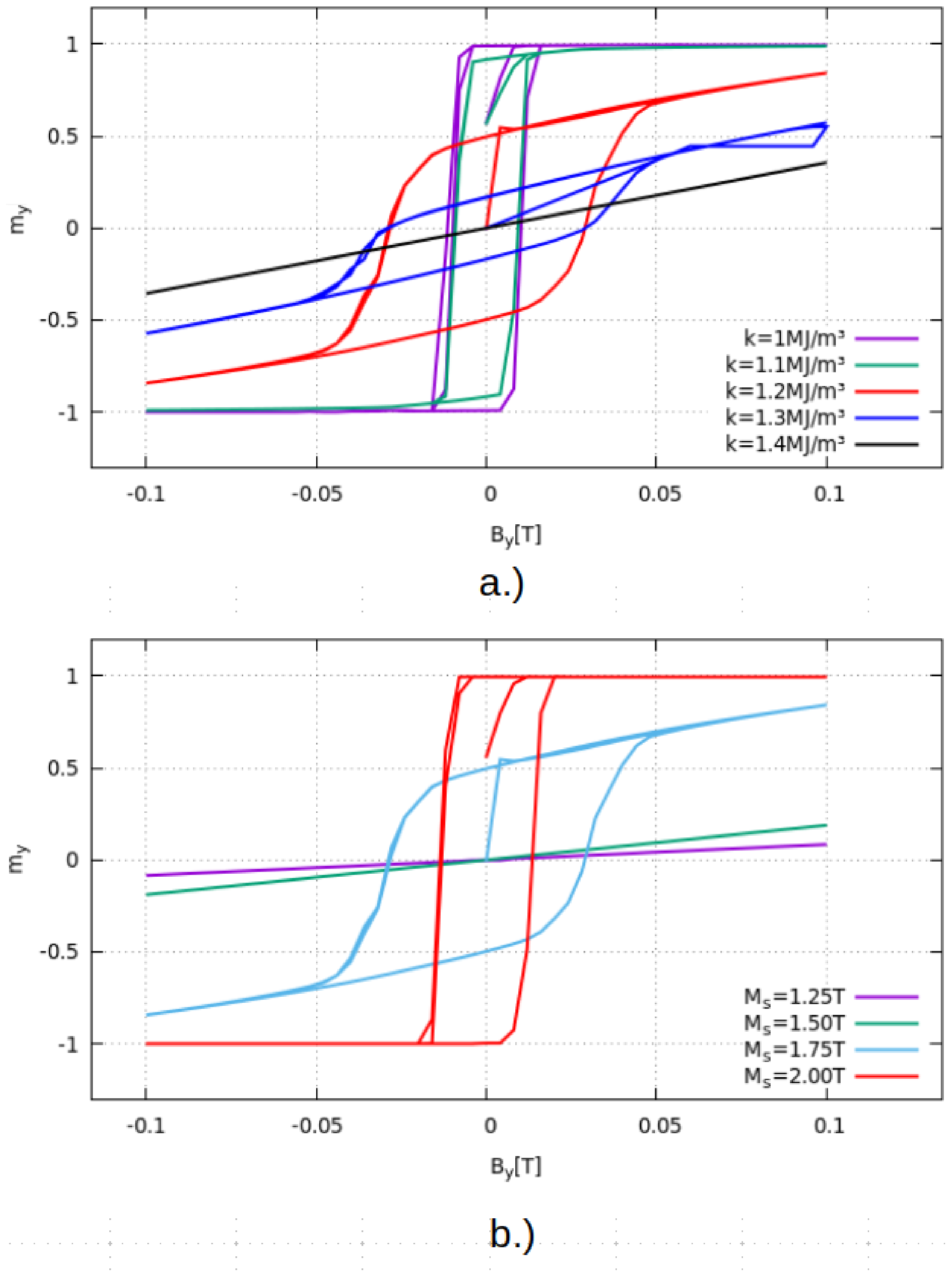

Figure 5.5: Hysteresis curves of the OOP sensor as a function of a.) the anisotropy constant k b.) the magnetization saturation M_s. The input values are taken from table 5.1 unless they are specifically stated in the legend

.

5.3 Checking the results using Stoner-Wolfarth

In this section we will try to give our results more validity by attempting to reproduce the stoner wolfarth-model. The Stoner-Wolfarth model was established in the previous chapter, it is applicable when magnetic structures exhibit uniform magnetic domains,in this case it is indistinguishable from micromagnetics. There are two ways that we are going to examine how well Stoner-Wolfarth is fulfilled. Firstly we are going to look at how well the equations that are established in chapter 4 are met. Additionally the Stoner-Wolfarth model predicts certain hysteresis for certain angles between the easy-axis and the applied field, therefore we can compare what Stoner-Wolfarth yields versus what we get with our micromagnetic simulation software. The equation that needs to be fulfilled are obtained by combining (4.6) and (2.28) which yields

$$k_{eff} = k_1 + k_{shape} = k_1 - \frac{J_s^2}{2\mu_0} \tag{5.1}$$

$$H_C = \frac{2k_{eff}}{\mu_0 M_s} \tag{5.2}$$

where k_{eff} is the effective anisotropy and H_C is the anisotropy field or in other words, as already shown, it is the field at which the sensor saturates. The only difference between (4.6) and (5.1) is the minus in front of the shape anisotropy. This is due to the fact that the shape anisotropy points in the negative z-direction. With the given parameters for the two sensors k_{eff} can be calculated and from that the anisotropy field H_C, the anisotropy field is the same as the magnetic field which needs to be applied in order to fully tilt the magneitzation, this can be checked with our micromagnetic difference code. The sensors for which this will be shown is the IP-sensor with $k = 1.0MJ/m^3$, the rest of the parameters needed for the simulation can be looked up in table 5.1. The same could of course also be done with an OOP-sensor.

The calculation yields $\mu_0 H_C = 313mT$, meaning that the magnetization should saturate in the z-direction at $B = 313mT$, in figure 5.6 it can be seen that simulating the SW model with micromagnetics leads to the correct hysteresis, since the magnetization saturates at $B = 300mT$, meaning that the equations are met. Stoner Wolfarth is of course capable of more than just predicting H_C, it can also yield the entire hysteresis curve. This was already shown before and can be looked up for various angles between the easy axis and the applied magnetic field θ in figure 4.4. Figure (5.6) shows the hysteresis for the simulation of such a sensor, one can see that it is in good agreement with the theoretical result from figure 4.4, meaning that the Stoner-Wolfarth model has successfully been reproduced.

5.4 Hysteresis with real matariels

In this chapter we will try to recreate hysteresis from [39]. The materials which is chosen to be simulated is Cobalt-Iron-Boron(CoFeB), a rare earth transition metal alloy.

In [39] magnetic tunnel junctions were fabricated by employing the material combination CoFeB-MgO. The material parameters used for the simulations can be looked up in table 3, and are also taken from the same paper. The crystalline anisotropy constant k depends on the thickness of the CoFeB layer t_{CoFeB}

$$k = \frac{k_i}{t_{CoFeB}} \tag{5.3}$$

with $k_i = 1.3MJ/m^2$. The comparison between the simulations and the experiments can be seen in figure 5.7. The in- and out of plane hysteresis was simulated for two different thicknesses, which are $t = 2.0nm$ and $t = 1.3nm$, by changing the thickness t one also changes the crystalline anisotropy constant k. Due to (5.3) with decreasing the thickness t one increases the anisotropy k in the z-direction which causes the in and out of plane loop to flip between the two thicknesses. That same phenomenon was simulated, which is illustrated in figure 5.7 . For $t = 2.0nm$ the out

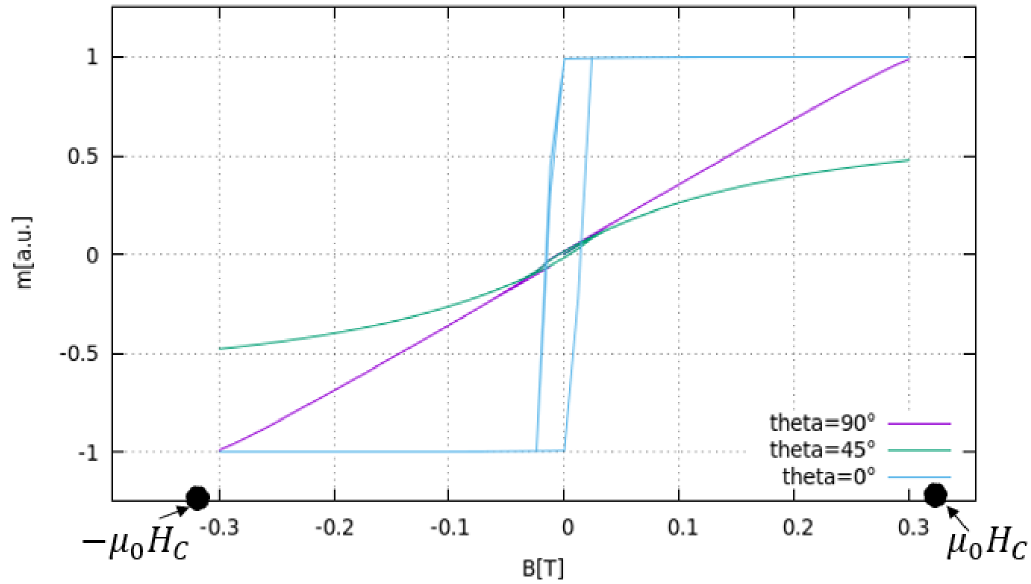

Figure 5.6: In order to check whether the micromagnetic software in use could replicate Stoner-Wolfarth, simulations for a material which has uniform magnetization were conducted where the angle θ between easy axis(=z-direction) and the applied field were changed for an IP-sensor with $k = 1.0MJ/m^3$. $\pm\mu_0 H_C$ were inserted in order to show that the stoner equations are fulfilled.

of plane loop from [39] has a linear form, this is also reproduced by our simulation, however it saturates at around $500mT$ whereas the experimental hysteresis saturates at $450mT$. The out of plane loop switches at zero field in the experiment[39], this is reproduced by our simulations. For $t = 1.3nm$ the simulated in plane loop matches better with the experiment since both simulation and experiment saturate at around $400mT$ for the out of plane loop, there is again switching at the zero field, which is also predicted by our simulations.

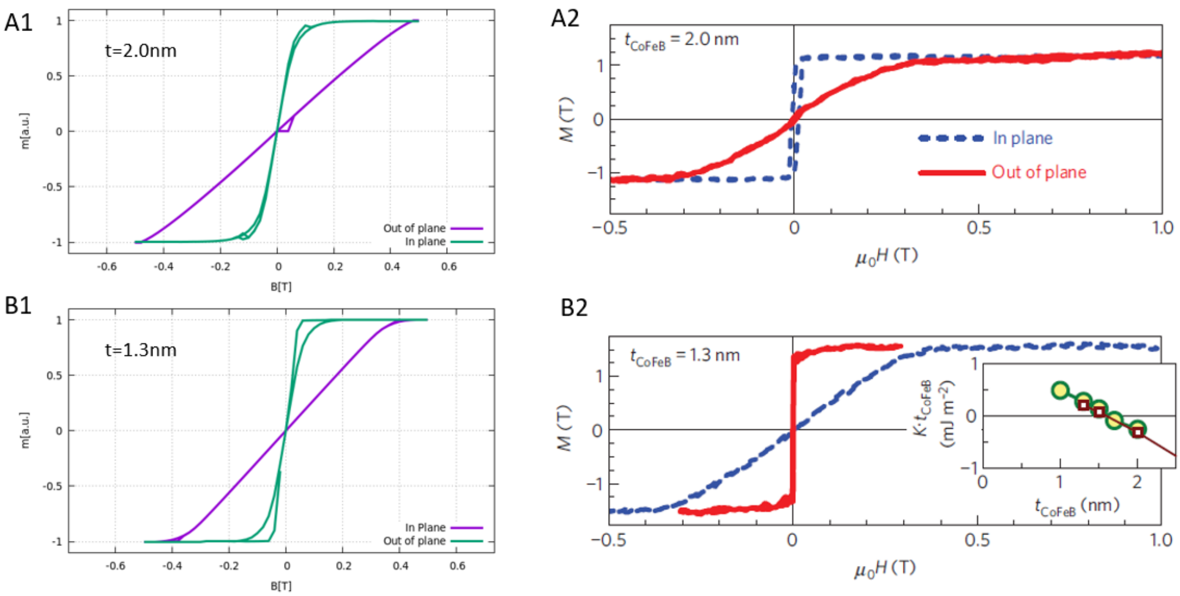

Figure 5.7: A comparison of simulated and experimental data of the perpendicular anisotropy sensors, for the $CoFeB$[39] alloy with the thicknesses $t = 1.3nm$,$t = 2.0nm$ was made. Graphs that have the same letter in their tag are to be compared with each other, graphs with "1" in their tag are simulations while graphs with "2" in their tag are experiments. A2,B2 are taken from [39].

Chapter 6

Angle sensing with perpendicular anisotropy devices

Magnetic angle sensors consist of a permanent magnet on a rotating shaft and one or more magnetic field sensors attached to a silicon die. The magnet is a diametrically magnetized pill, meaning that it is a cylindrical magnet, whose magnetization points in plane, as can be seen in figure 6.5. The magnetic sensors are supposed to detect the field of the rotating magnet and conclude back the angle of rotation. This part of the thesis will focus on how such a sensing concept can be implemented using magnetic sensors which utilize perpendicular magnetic ansiotropy and the errors which arise from the sensor elements themselves and assembly tolerances. Let us again shortly sum up our findings before we discuss the results in detail.

The first thing that has to be considered is the placement of the sensors relative to the magnet, this is what we refer to as sensor configuration. The configuration for the sensors differs for the two sensor designs. For the OOP case we place the sensor centrally above the magnet, which we refer to as the axial setup, for the IP case we place 4 sensors above the magnet in a circle with a phase shift of $90°$, which is called the differential setup, both setups are illustrated in figure 6.2.

In order to have functioning sensors one would like to have magnetic materials which are single domain throughout their entire hysteresis and additionally we would like for our sensors to have the same linear range for the sake of comparability. In order to obtain both, the stoner-wolfarth model was again used to calculate the crystal anisotropy k for a sensor that would saturate at $100mT$, how to calculate this in detail is explained within one of the following chapters.

The first simulations of these sensor devices as angle sensors can be seen in figure 6.4. The OOP sensor shows no angle error, however the IP sensor shows a significant angle error. The error of the IP sensor was simulated for different positions of the four sensors. This can be seen in figure 6.6. Through that we show that the IP sensor can be used as an angle sensor in the differential setup if the applied in plane magnetic fields are constant, which is only true for certain positions.

As a next step different external error sources were implemented in order to see how they effect the angle sensing performance. Firstly a mechanical stress was implemented by applying a uniaxial anisotropy of $k_s = 1.4kJ/m^3$ in the in plane direction. Figure 6.7 shows the angle error when being subject to an additional anisotropy generated by a mechanical stress, where the OOP sensor error increases significantly while the IP sensor remains unchanged. Secondly bias fields were applied in out of plane and in plane directions, as can be seen in figures 6.8, 6.9 and 6.10. For out of plane bias fields the errors remain unchanged, whereas with in plane fields the angle error for all sensors increases significantly. Finally the IP and OOP sensors were offset in plane, which basically means that the entire sensor configuration was moved in the x-direction relative to the magnet. This of course gives an angle error that even the most perfect angle sensor would show, since the magnetic field that the sensor is subject to changes. This is shown in figure 6.12 for the IP sensor and in figure 6.13a.) for the OOP sensor. The solution is then shown in figure

6.14 and 6.13b.) where one can see that a relatively low angle error is given for an offset of up to $0.9mm$ if the right position for both sensors is chosen.

Lastly an autocalibration was implemented, in order to nullify the external errors, as can be seen in figures 6.15 and 6.16. The autocalibration worked well for the OOP sensor however not so much for the IP sensor.

6.1 Sensor Magnet Setup

Let us first discuss how to setup our magnets to our sensors because it is not as straightforward as one may think.

Lets begin with our OOP-sensor, since it is the more obvious one. Let me just mention here,as a quick reminder that the OOP sensor is sensitive to in-plane fields, and its fixed layer is in plane.

The OOP sensor will be placed centrally above the magnet. At this position it will recieve a circular field of the form

$$\vec{B} = B \cdot \begin{bmatrix} cos\phi \\ sin\phi \\ 0 \end{bmatrix} \tag{6.1}$$

With B being the amplitude of the field and ϕ being the angle of the magnet, which is also the value one wants to measure. Ideally the magnetization, which is subjected to such a field, should have a similiar form

$$\vec{m} = m \cdot \begin{bmatrix} cos\phi \\ sin\phi \\ 0 \end{bmatrix} \tag{6.2}$$

If this is the case one can simply use the arcus-tangent of the x- and the y-signal and thereby calculate the magnetic field

$$\phi = atan\left(\frac{m_x}{m_y}\right) = atan\left(\frac{sin(\phi)}{cos(\phi)}\right) \tag{6.3}$$

Since one sensor can only measure one component, we actually need to place 2 sensors centrally above the magnet right next to each other, as can be seen in figure 6.2 a.), in this figure the 2 sensors are drawn eccentrically far apart from one another for the sake of clearity, in reality those sensors would be as close to each other as technically possible. We will refer to this setup as the axial setup.

Let us now discuss how to setup our IP sensors. One might naively try to implement this sensor the same way as it was set up for the OOP sensor. However this would be nonsensical because this would mean that the magnetization would be in the plane, if this were the case the perpendicular anisotropy would never be triggered meaning that the sensor would work as a simple MR-angle sensor. One might jump next to a solution where the field is not applied along the x-y plane but along the y-z or x-z plane in order to utilize the magnetic anisotropy. However this is also not a viable solution, because if one wants to measure the angle of the magnetization in a plane the anisotropy should be the same in all direction of that plane. This is true for the OOP sensing setup because the measuring plane is subject to the shape anisotropy in all directions of that plane. If one were to utilize the y-z plane for the IP sensor, the anisotropy in z direction would be that of the crystalline magnetic anisotropy and the y-direction would have the shape anisotropy. One might try to make these anisotropies equal, however in that case one would open a whole other source of errors.

The solution is inspired by [41]. 4 IP sensors are placed above the permanent magnet in a circle with a phase difference of $90°$ between the individual sensors. Two parameters are crucial when talking about this setup , firstly the leseradius(=lr), which is the distance from the centre of that circle to the sensors, and secondly the airgap(=ag) which is the distance between the surface of the magnet and the circle which is formed by the sensors, as can be seen in figure

6.1, additionally 6.2 b.) gives a 3-dimensional view of the setup. The magnetic signals in the z-direction can be written as

$$\begin{aligned} m_{1,z} &= mcos(\phi) \\ m_{2,z} &= msin(\phi) \\ m_{3,z} &= -mcos(\phi) \\ m_{4,z} &= -msin(\phi) \end{aligned} \tag{6.4}$$

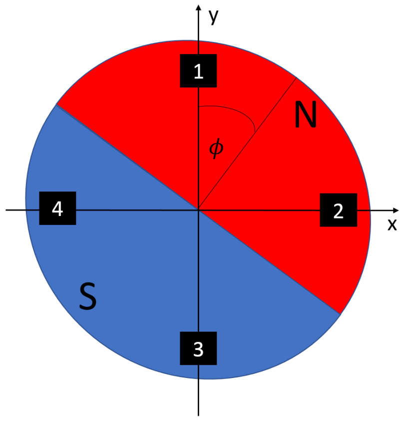

Figure 6.1: Schematic showing the positions of the 4 IP-sensor in the differential setup relative to the cylindrical magnet that is turned by ϕ, the magnetization signals $m_{i,z}(\phi)$ are as shown in (6.4).

Next the angle can be calculated by computing the differences of the opposing signals and afterwards again evaluating the arcus-tangent of the fraction

$$\phi = atan\left(\frac{m_{2,z} - m_{4,z}}{m_{3,z} - m_{1,z}}\right) = atan\left(\frac{sin(\phi)}{cos(\phi)}\right) \tag{6.5}$$

Technically not all four sensors are needed, to simply measure the angle 2 would suffice, however using 4 can become advantageous when external errors are introduced, for example homogeneous bias fields in z-direction would be compensated by using 4 instead of 2 sensors. In the following we will refer to this as the differential setup.

6.2 Sensor Parameters

For angle sensing we would like to our sensors to exhibit a shape anisotropy which is the same along every direction in plane of the sensor, in order to obtain this we will change from our elliptic form to a circular form with a diameter of $800nm$. Our sensors are also required to have uniform magnetisation and should saturate at around $100mT$. In order to obtain this the Stoner-Wolfarth model is applied, to calculate our perpendicular crystalline anisotropy k. We will use the same equations as before but manipulate them slightly to get an equation for the anisotropy.

$$k = \pm k_{eff} - k_{shape} = \pm\frac{H_c J_s}{\mu_0 2} + \frac{J_s^2}{2\mu_0} \tag{6.6}$$

the only thing of note that has changed is that we have to be careful with the sign of the effective anisotropy k_{eff}. The sign of k_{eff} did not matter before, because it only affected wether

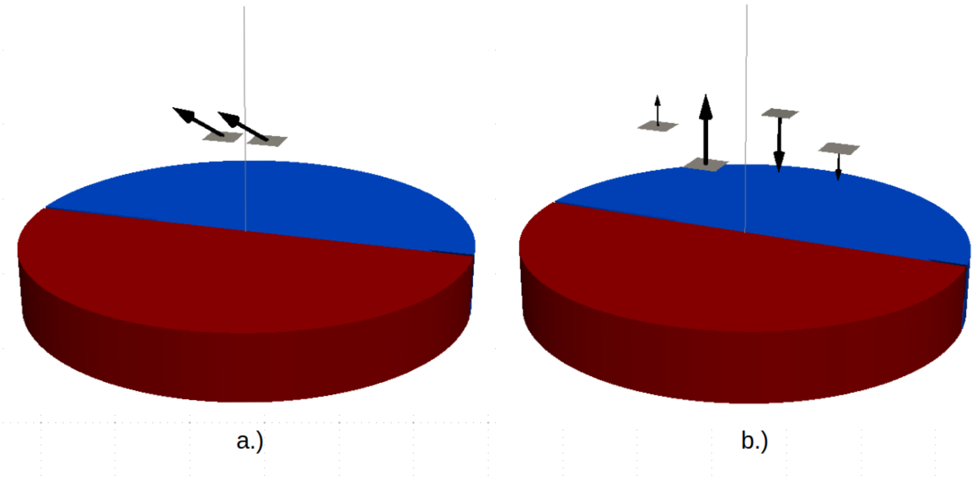

Figure 6.2: The setups for magnet to sensors for our two distinct sensors a.) the OOP sensor has the axial setup where two sensors are placed centrally, with a certain airgap above the magnet b.) the IP sensor has the differential setup where the sensors are placed in a circle with a certain distance from the central point (=leseradius) and with a gap between the circle formed by the sensors and the magnet (=airgap). The black arrows represent the direction of the magnetization for a certain magnetic field.

	OOP	IP	Vortex
$k[MJ/m^3]$	1.0	0.079	\
$J_s[T]$	1.53	0.5	1.75
$A[pJ/m]$	15.0	15.0	15.0
$t[nm]$	1.3	3.5	65
$D[nm]$	800	800	800
Geometry	Disk	Disk	Disk

Table 6.1: The table shows the input values which have led to the hysteresis shown in figure 6.3

H_C is positive or negative, however wether we assume k_{eff} to be positive or negative changes the value of k. If we want to calculate k for the OOP sensor we assume that $k_{eff} > 0$ because the magnetization points out of plane, and we assume $k_{eff} < 0$ for the IP sensor because the magnetization points in plane.

For the OOP sensor we will use the saturation magnetization M_s and exchange constant A from table 3. Using the equation from above, where we choose k_{eff} to be positive it yields $k = 1.0MJ/m^3$. We use table 4 to obtain all the necessary data to calculate k, where we choose k_{eff} to be negative, this yields $k = 79kJ/m^3$.

In figure 6.3 the hysteresis for these materials with the newly calculated k can be seen, in addition to the vortex sensor which is shown for comparisons sake. The input values which have led to these hysteresis are shown in table 6.1. Since the hysteresis are quite similiar, these three sensors are quite comparable when it comes to angle sensing.

6.3 Simulating perfectly aligned angel sensors

To start off we will simulate perfectly aligned sensors, meaning the only error comes from our sensor performance, without any external sources, because we want to make sure our concepts work.

The magnetic field $\vec{B}$ which is input into the simulation obviously varies for the two sensor concepts. For OOP we approximate the field with (6.1). This is quite accurate since centrally above such a magnet the field looks exactly like this, the only discrepancy is that we don't have one sensor positioned above, but two next to each other, meaning that both sensors get a slightly

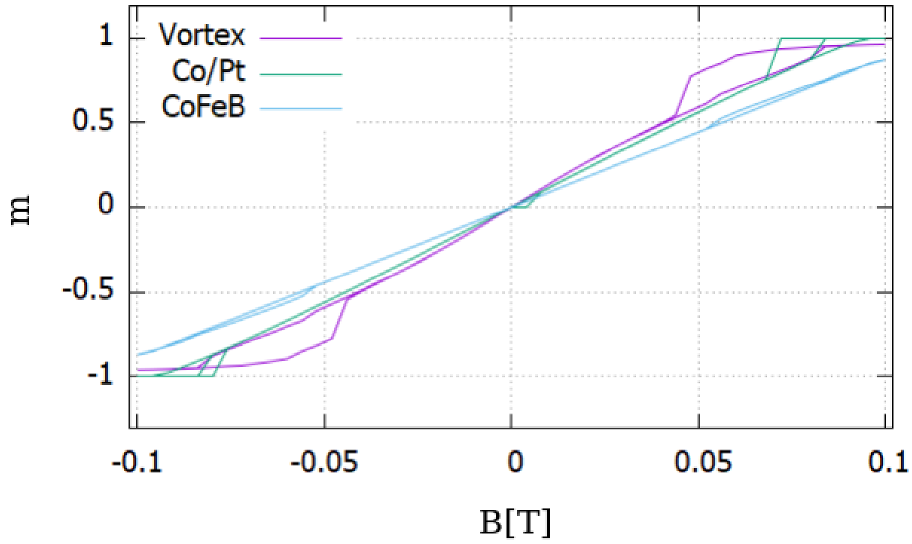

Figure 6.3: The hysteresis curves for the three sensors, of which there are the Co/Pt sensor which is used as an IP-sensor, the CoFeB sensor which is here being utilized as an OOP sensor and the vortex sensor which is used as a comparison to the other two.

different field, however this difference is negligible and will be dealt with later on.

In order to simulate the IP sensor we approximate the magnetic field $\vec{B}$ with a magnetic dipole

$$\vec{B} = \frac{\mu_0}{4\pi} \frac{3\vec{r}(\vec{r} \cdot \vec{m})}{|\vec{r}|^5} - \frac{\vec{m}|\vec{r}|^2}{|\vec{r}|^5} \tag{6.7}$$

this approximation makes sense since in a far enough distance the magnet and the dipole field do look exactly the same, however this approximation is no longer valid if we start talking about misalignment or similar issues, but in order to test our concepts it will suffice.

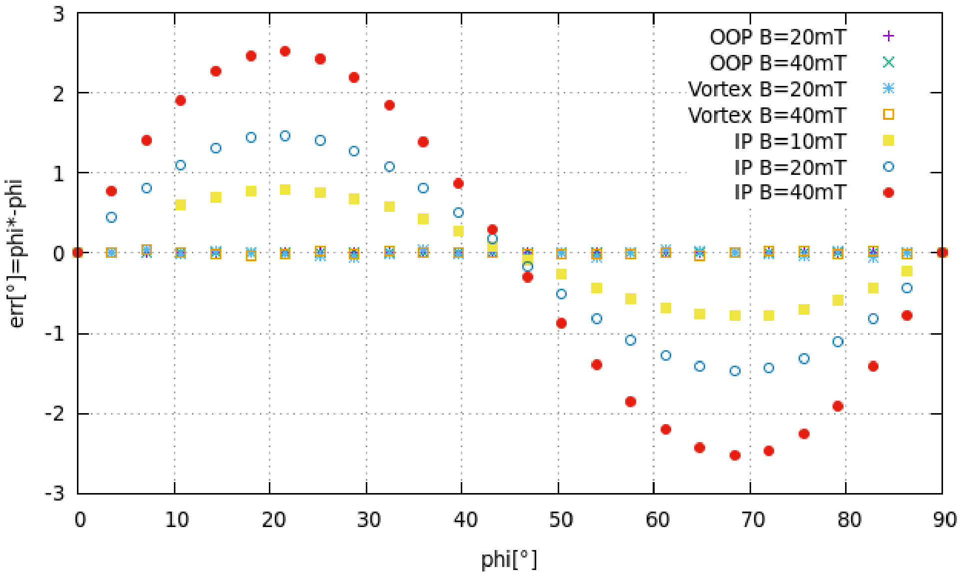

Figure 6.4: The angle-error, meaning the difference between the actual angle of the magnet ϕ minus the measured angle ϕ' of different angle sensing concepts and different magnitudes of the magnetic field were simulated and plotted against the actual angle.

Figure 6.4 shows the angle-error of the individual sensor concepts, where B denotes the maximum field which is applied. Vortex and OOP exhibit no angle error independent of how big the field is, however the IP sensor shows a significant angle error around and above $1°$ for all applied fields, with a smaller field yielding a smaller angle error, which is unintuitive, considering that sensors usually work better when the applied magnetic field $\vec{B}$ increases. However this train of thought doesn't work in this case. The 4 IP sensors are subjected to fields which they don't measure, namely in-plane fields. Since the sensor is circular, only the transversal component $B_{trans} = \sqrt{B_x^2 + B_y^2}$ is relevant, additionally the transversal field can be looked at, as an additional in plane anisotropy. The transversal field is not constant for every angle, which means that every one of the 4 sensors has a different in-plane anisotropy, which yields this high error. Therefore one would have to find a position where $B_{trans} = const. \ \forall \, \phi$, in order to do that we created a phase plot where the maximum angle error is plotted against $leseradius$ and $airgap$. The contour plot is shown in figure 6.6a.). One can see that the angle error goes towards zero if the transversal field is constant for all angles ϕ of the magnet, it is also evident that there is a line where this condition is met, one can calculate analytically where the transversal field is linear, a solution is that it is linear for $\sqrt{2}lr = ag$, which is the dashed line in figure 6.6a.). The areas with angle errors exceeding $1°$, are either due to the field being bigger than the sensing regime, meaning $B > 100mT$ or due to a very non-linear transversal field.

Now that we have found a way for all our sensors to have angle errors that are near zero, we move away from the dipole approximation in order to implement a real magnetic field. The material that was chosen for the permanent magnet is NdFeB with a saturation magnetization of $M_s = 1.6T$[40] in the form of a cylinder with a diameter of $6mm$ and a thickness of $2.5mm$. The magnetic field was calculated by calculating the demagnetizing field of such a geometry in an airbox with magnum.af.

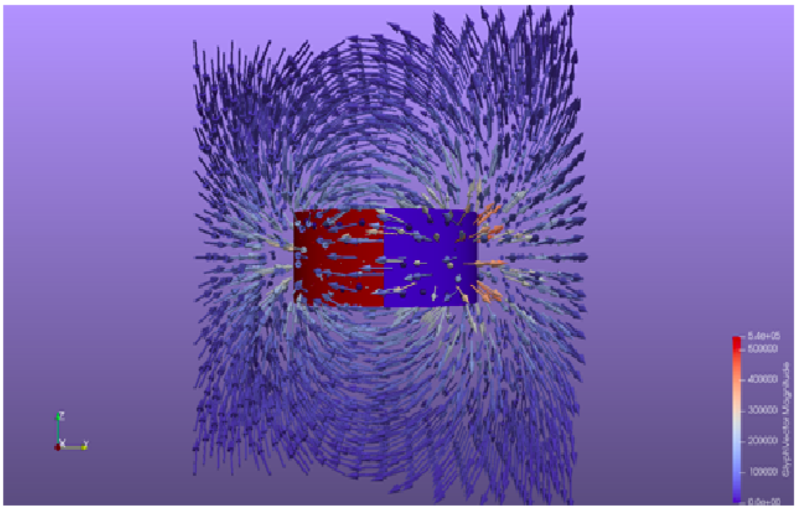

Figure 6.5: A cylindrical magnet with an in-plane magnetzation of $M_s = 1.6T$, a diameter of $6mm$ and a thickness of $2.5mm$ was simulated in order to obtain the true field an in plane sensor in differential setup would be subjected to.

In figure 6.5 one can see the magnetic field which is generated by a magnet as it is described above and figure 6.6b.) shows the angel error, when the sensors are being subjected to a field as shown in figure 6.5, as a function of the leseradius and airgap of our sensor setup, again the applied field is inserted for certain positions of the sensors. It becomes again apparent that the angle error is around zero when the transversal field is constant. We omitted showing the angle error for the Vortex and OOP sensor being submitted to a real magnet, because the difference is not noticeable. We have now shown that our two perpendicular anisotropy angle sensing concepts exhibit angle error of zero when being submitted to a real magnet and the positions are chosen properly.

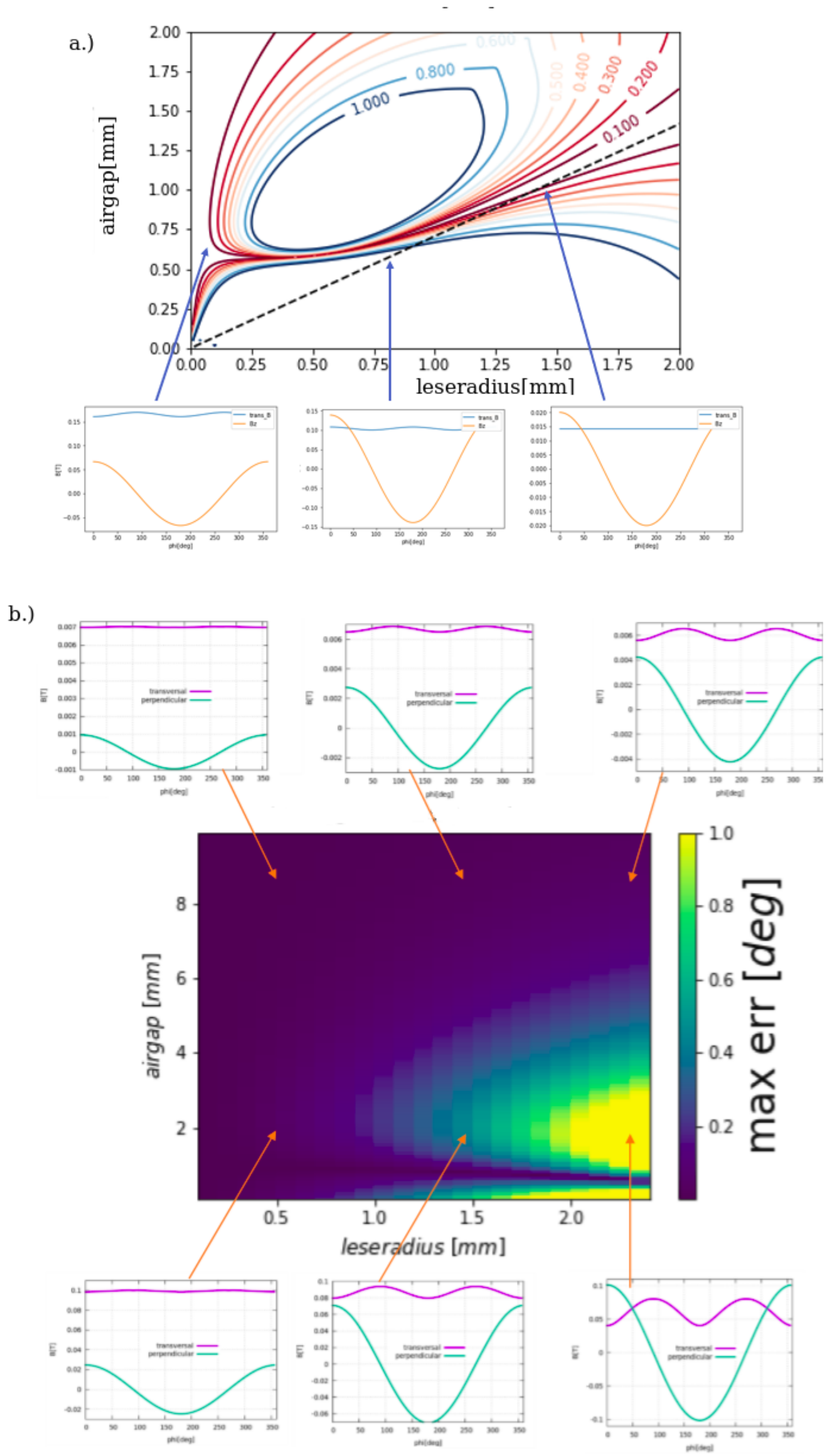

Figure 6.6: The angle error of the IP sensor, in the differential setup, as a function of the leseradius and the airgap was calculated with a.) the field approximated by a magnetic dipole. The angle errors are near zero are when $B_{trans} = const.$, additionally a dashed line was added which shows where $ag = \sqrt{2}lr$, which is where the condition for $B_{trans} = const.$ is met b.) the field of a cylindrical magnet with the magnetization in plane, again angle errors are near zero for fields that are constant in plane. The perpendicular and transversal fields were added at certain positions to again emphasize the dependence of the angle error on the applied fields.

In the next chapters we will discuss what happens if they aren't perfectly aligned but exhibit imperfections which give rise to further angle errors.

6.4 Stress induced anisotropy

Whenever a ferromagnetic sensor is attached to a wafer it will be subject to a mechanical stress, which means that in turn it will gain a uniaxial anisotropy which could potentially be a source for angle errors. Bachleitner[28] compared the anisotropy fields of large unstructured wafer fragments which have been put under mechanical stress in experiments to micromagnetic simulations of a CoFeB film, which brought him to the conclusion that the mechanical stress can be simulated by applying an additional anisotropy of $k_S = 1.4kJ/m^3$ which is directed in plane. Figure 6.7 shows the simulation results for the different sensor concepts when they are being subject to a stress induced anisotropy $k_S = 1.4kJ/m^3$. Both the Vortex and the OOP-sensor show a significant increase in angle error from $0°$ to around $0.6°$, with the maximum error being around $\phi = 45°$. This shape can be explained by looking at the angles between the stress induced anisotropy and the external field. As already mentioned we can think of the stress as an additional anisotropy in plane therefore we can write the stress-induced anisotropy field

$$\vec{H}_{ani} = k(\vec{e}_{ani} \cdot \vec{m})\vec{e}_{ani} \tag{6.8}$$

$$\vec{H}_S = k_S(\vec{e}_S \cdot \vec{m})\vec{e}_S \tag{6.9}$$

If there is no stress being applied to the sensor the magnetization always aligns parallel to the external field. If the stress is applied parallel to the external field meaning $\vec{H}_S || \vec{H}$ then we have no angle error since the magnetization is already along the direction favoured by the stress, in figure 6.7 this is the case at $\phi = 0$. In case the external field is perpendicular to the field $\vec{H}_s \perp \vec{H}$ the scalar product becomes zero and the angle error vanishes, meaning that the maximum error must be right inbetween those two angels which is $\phi = 45°$, which is exactly what the figure 6.7 is showing.

Additionally the OOP and Vortex sensors seem to be indifferent to the magnitude of the field which is applied. Looking at the average anisotropy field

$$\langle \vec{H}_S \rangle = \langle k_S(\vec{e}_S \cdot \vec{m})\vec{e_s} \rangle = k_S(\vec{e}_S \cdot \langle \vec{m} \rangle)\vec{e_s} \tag{6.10}$$

it is obvious that the anisotropy field is liner in $\langle m \rangle$ meaning that an increase in the anisotropy field, automatically causes an increase in the average magnetization $\langle \vec{m} \rangle$ hence the angle error is independent of the applied field.

For the IP sensor in differential setup the stress seems to make no difference. The IP sensors are not measuring in plane fields, but only out of plane fields, meaning that an additional anisotropy in plane should not affect the angle error whatsoever, as can be seen in figure 6.7.

6.5 Bias field

A sensor in application could very well be exposed to various stray fields which result in an effective bias field, especially in the automotive industry, where other magnetic devices might be in operation. For this case we will treat in plane biases and out of plane biases separately, since our sensors are energetically symmetric in plane this is a sensible approach.

Out of plane bias field

An out of plane bias field does not affect the IP sensor in the differential setup. When a bias field $\vec{B}_{b,z}$ is applied in z-direction, the magnetic field which is of sine- or cosine form is raised

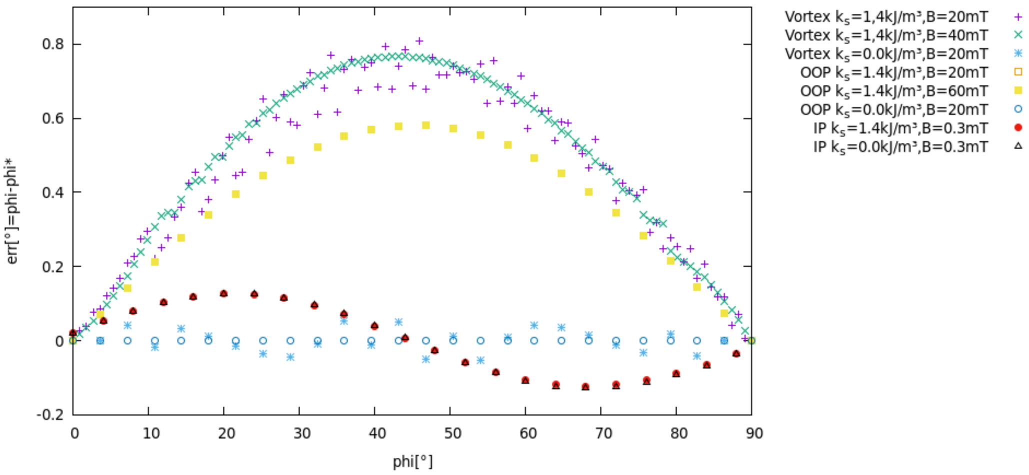

Figure 6.7: Mechanical stress is being simulated by adding another in plane anisotropy of $k_s = 1400kJ/m^3$ to all three sensor concepts.

$B_{1z} = Bcos(\phi) + B_{b,z}$, which also raises the magnetization $m_{1z} = msin(\phi) + m_{b,z}$ however the differential setup cancels this out. We write the "corrupted" angle ϕ' as

$$\phi' = arctan\frac{msin(\phi) + m_{b,z} - msin(\phi) - m_{b,z}}{mcos(\phi) + m_{b,z} - mcos(\phi) - m_{b,z}} = arctan\frac{sin\phi}{cos\phi} = \phi \tag{6.11}$$

This can be seen in figure 6.8.

The OOP-sensor is also not affected by out of plane bias fields but for completely different reasons. Having a constant field in z-direction, will simply tilt the magnetization towards the z-direction, however these sensors are sensitive to in-plane fields meaning the tilt towards the z-direction doesn't change the angle the OOP sensor yields, as can be seen in figure 6.8.

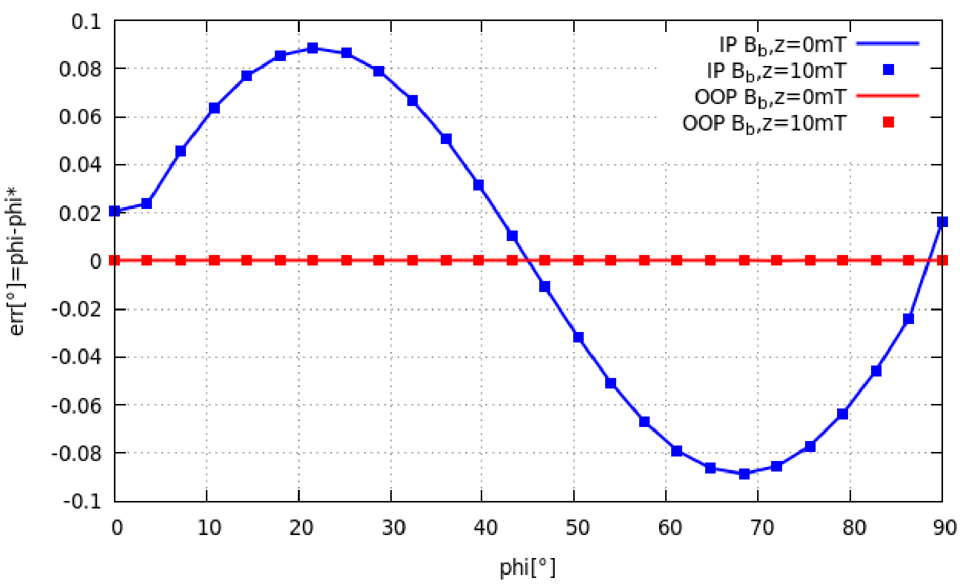

Figure 6.8: An out of plane bias field $B_{b,z} = 10mT$ has been applied to both sensor concepts. The angle error is unaffected by the bias fields, if they are applied along the z-direction.

In plane bias fields

In plane bias fields $\vec{B}_b$ are much more significant for the sensors at the heart of this work. IP sensors will exhibit an increase in angle error because the transversal field $\vec{B}_{trans,bias}$ is not constant anymore

$$\vec{B}_{trans} = \sqrt{B_x^2 + B_y^2} = \sqrt{(B_a sin\phi)^2 + (B_a cos\phi)^2} = B_a = const. \tag{6.12}$$

$$\vec{B}_{trans,bias} = \sqrt{(B_x + B_b)^2 + B_y^2} = \sqrt{B_a^2 + 2B_a cos(\phi) B_b + B_b^2} \neq const. \tag{6.13}$$

where B_a is the amplitude of the applied in plane fields. This increase can be seen in figure 6.9 for $B_a = 15mT, B_b = 2mT$. This error can be reduced if a position is chosen, where the amplitude B_a of the magnetic field is increased, as can be seen by the low angle error in figure 6.9 for $B_a = 100mT, B_b = 2mT$. 1D-Hall sensors are only sensitive to the sensing direction. Therefore if one were to utilize Hall sensors, which are sensitive to out of plane magnetic fields, in the differential setup, an in-plane bias would not affect the angle error. This is also shown in figure 6.9.

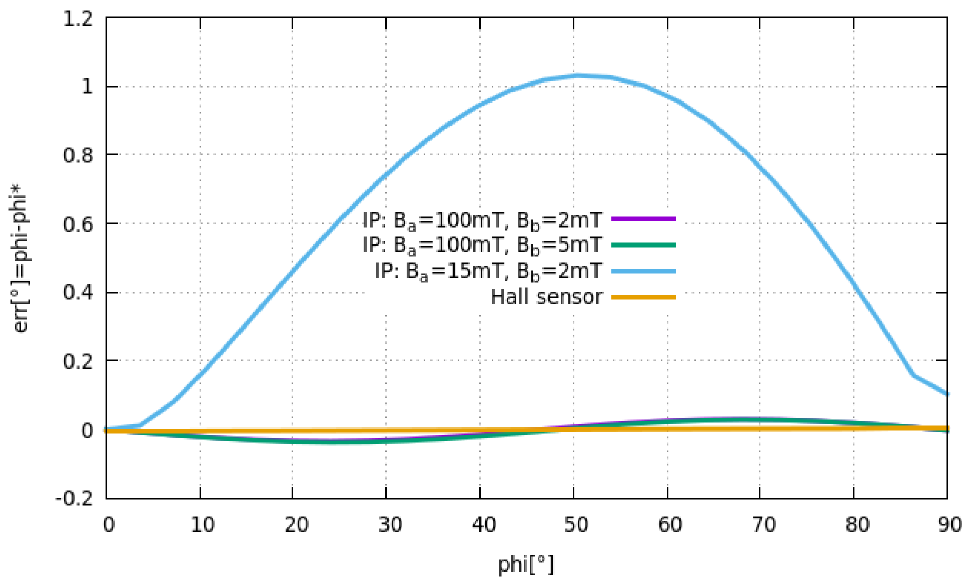

Figure 6.9: An in plane bias field of $B_b = 10mT$ has been applied to the IP-sensor. For comparison sake the angle error for a Hall sensor under the same bias-field is also shown.

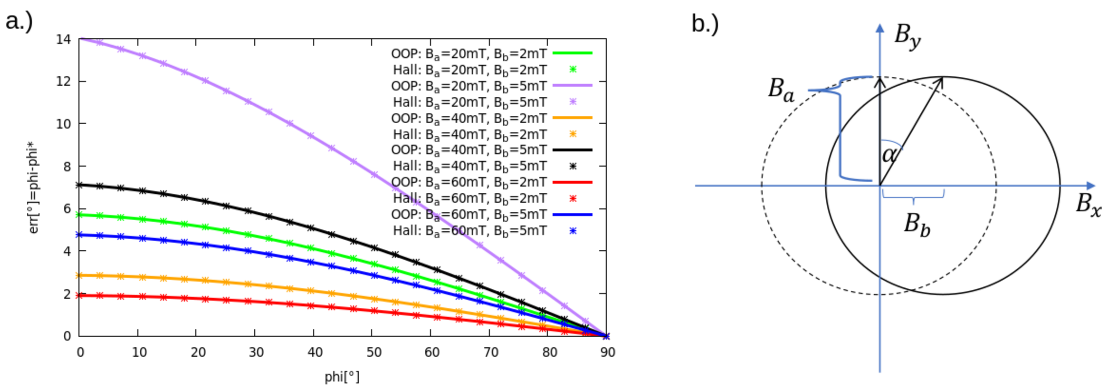

Figure 6.10: a.) Various out of plane bias fields have been applied to the OOP sensor, in order to study the error-dependence of the bias field. b.) When a bias field $\vec{B}_b$ is applied to the axial setup, the entire sensing plane is shifted, meaning that even a Hall sensor yields a significant angle error.

For the OOP-sensor the rotational field is being offset by a bias field vector $\vec{B}_b$ in the $B_x - B_y$ diagram, as can be seen in figure 6.10 b.). If the field is parallel to the bias, the angle error will vanish and if the field is perpendicular to the bias field the error can be easily calculated with $err = 90 - atan(B_a/B_b)$, where B_a is the amplitude of the rotational field. For a bias of $2mT$ and an amplitude of $20mT$ we get an error of $5.8°$, as seen in figure 6.10 a.). This error can of course be reduced by introducing a bigger amplitude, however one is limited by the linear range of the sensor. Implementing 1D-Hall sensors with the axial setup will always yield the same error as the OOP sensor, since the entire sensing plane is moved by $\vec{B}_b$, this is illustrated in figure 6.10 a.).

6.6 Sensor offset

Whenever sensor systems are being assembled there is always the possibility for manufacturing errors, a very common one is the sensor offset. A sensor is offset if it's position relative to the magnet is shifted with respect to its ideal position. Here we will only take into consideration offsets along the x-y plane and since we have an in plane symmetry it doesn't make a difference in which direction the sensor is offset. z-directions are being ignored since moving any of these sensors along the z-direction results in nothing but changing the magnitude of the magnetic field, and this effect has already been discussed.

Let us begin by discussing the IP sensor being offset in x-direction theoretically. Figure 6.11 a.) shows a schematic for a perfectly aligned sensor with leseradius lr , while 6.11 b.) shows a sensor which is offset by off. Therefore the magnetic field that two of the four sensors recieve is phase shifted by α.

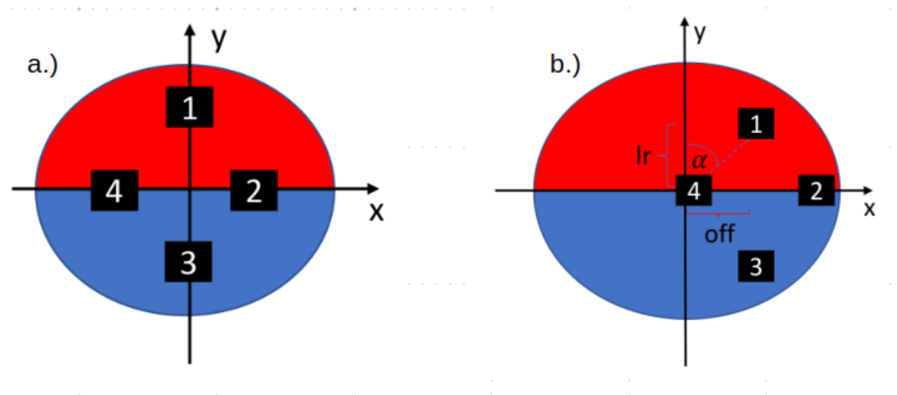

Figure 6.11: a.) Perfectly aligned sensor with leseradius lr b.) Sensor offset by off in x-direction

To understand how the magnetic signals change qualitatively we consider sensor 1 as it is shown in figure 6.11 a.). If we use the same origin and denote the position $\vec{r}_1$ of sensor 1 in polar coordinates we can write them as $\vec{r}_1 = (lr, 90)$, where lr denotes the leseradius, we ignore the z-component the sensor obviously has in this example, since it doesn't transform under an offset in x-direction. If the sensor is offset in positive x-direction we can write the altered position as $\vec{r}_1' = (lr + x, 90 - \alpha)$, where x is a certain distance. By the change in angular coordinate the field will also exhibit a phase shift by α and changing the radial coordinate will alter the amplitude of the magnetic signal. This yields

$$\begin{aligned}B_{1,z} = Bcos\phi \Rightarrow B'_{1,z} = B_A cos(\phi + \alpha)\\ B_{2,z} = Bsin\phi \Rightarrow B'_{2,z} = B_B sin\phi\\ B_{3,z} = -Bcos\phi \Rightarrow B'_{3,z} = -B_A cos(\phi - \alpha)\\ B_{4,z} = -Bsin\phi \Rightarrow B'_{4,z} = -B_C sin(\phi)\end{aligned} \tag{6.14}$$

where $B'_{i,z}$ is the altered magnetic field at the offset position. We further write

$$
\begin{aligned}
B_{1,z} - B_{3,z} = B_A cos(\phi + \alpha) + B_A cos(\phi - \alpha) = 2B_A cos(\alpha) cos\phi \\
B_{2,z} - B_{4,z} = (B_B + B_C) sin\phi
\end{aligned}
\tag{6.15}
$$

$$
\phi \approx atan \frac{(B_B + B_C) sin\phi}{\frac{B_a cos\alpha}{2} cos\phi} = C * \frac{sin\phi}{cos\phi} \tag{6.16}
$$

$$
C = \frac{B_B + B_C}{2B_A cos(\alpha)} \tag{6.17}
$$

C can be seen as an indicator for how big the angle error will become and since C is directly linked to the error induced by the offset we call C the offset-factor, for a low angle error the offset-factor needs to be $C \approx 1$. Keep in mind that in these past equations we have exclusively been talking about the magnetic field, meaning that this error source does not exclusively depend on sensor performance but on the overall design of this sensor setup. To really grasp what this means let us consider a perfect magnetic sensor. A perfect sensor always aligns its magnetization perfectly along the components of the magnetic field which it measures. The Hall sensor has such properties. Therefore if we have 4 Hall sensors which are offset by a certain distance, although they perfectly measure the magnetic field, they would still exhibit a systematic angle error, due to the fact that they measure the magnetic fields at wrong position. This is why in this chapter the error an IP- or OOP sensor exhibits under a certain offset, will be compared to the error perfect/Hall sensors would make.

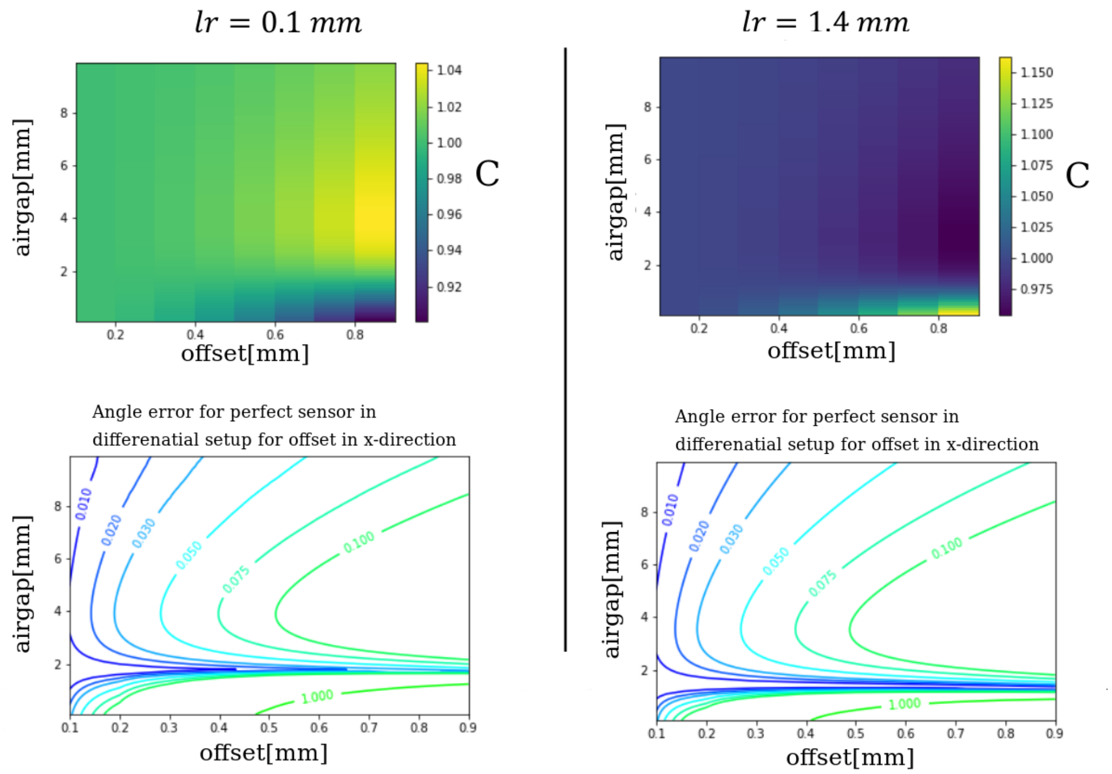

Figure 6.12: Phase plots and contour plots for C and H_z-error respectively with $lr = 1.4mm$ and $lr = 0.1mm$, since the plots are quite similiar it is quite obvious that the deviation from $C = 1$ is a good indicator for the error produced by the magnetic field H_z-error.

Furthermore we could have just as easily substituted the magnetic field with the magnetization in the above equations and it would have been just as true. Figure 6.12 shows the dependence of C and the angle error of a perfect/Hall sensor on offset and airgap for the different leseradius $lr = 0.1mm$ and $lr = 1.4mm$. One can sumize that the change in leseradius doesn't effect the error since both contour plots for $lr = 0.1mm$ and $lr = 1.4mm$ are identical. Additionally the notion that the deviation from $C = 1$ is an indicator for the magnitude of the error of the magnetic field is proven because the phase plots for C and the H_z-error are identical.

Figure 6.14 shows the IP-sensor errors when being offset for varying leseradius and airgaps. For $lr = 0.1mm$, $ag = 1.0mm$ one can see that when not being offset this position has an angle error around zero, this can also be seen in the phase plot a.) at the position which is marked with an orange marker, however the orange line for b.) shows that this position when being offset will submit large angle errors due to the magnetic field being misaligned, e.g. a misalignment of $0.6mm$ already yields a 1° angle error from the magnetic field alone.

The configuration $lr = 0.1mm$, $ag = 2.0mm$ will again give a vanishing angel error when it is perfectly aligned. Additionally it sits in a sweet spot where even if the sensor is offset by $0.9mm$ the sensor only has an angle error of 0.32°, which is relatively low. However as can be seen in the blue line in b.) this sensor configuration sits at a point where all the lines for the different angle errors intersect, which means that even if this sensor has a slightly different airgap than $ag = 2.0mm$ it could mean a drastic increase in angle error.

A sensor sitting at $lr = 1.4mm$, $ag = 2.0mm$ will also have an angle error around zero, however in a.) the position of the sensor is marked with a red dot, one can see that this sensor lies at a position where all the contour lines lie very close next to each other, meaning that again a slight misaligned airgap could mean a drastically different angle error, Additionally the error highly increases when being offset, which is partly due to the error of the field as can be seen by the red line in c.) and also potentially due to the fact that if the offset gets that big the sensor gets pushed more towards a position where the transversal field is not linear anymore.

Decreasing the airgap to $ag = 1.0mm$ and leaving the leseradius at $lr = 1.4mm$ will leave the sensor with a non vanishing angle error, as can be seen in a.) where the position was marked with a green dot. This is caused by the nonlinearity of the transversal field at this point. However as can be seen with the green line in c.) the sensor sits slightly above where all the contour lines meet meaning that the offset doesn't influence the angle error as much as it does with the other positions.

If a sensor in the axial setup is offset it will also yield an error, even if the sensor perfectly aligns its magnetization along the applied magnetic field, this is shown in figure 6.13a.). The error made by the perfect sensor is heavily dependent on the airgap that is chosen. For $ag = 1mm$ the error is significantly lower than for bigger airgaps. However the errors seem to decrease for an increasing airgap. The angle error an OOP sensor makes when offset is shown in figure 6.13b.), where it is shown that the trend predicted by the error for a perfect sensor shown in figure 6.13a.) is reproduced. Meaning that for $ag = 1.0mm$ the OOP sensor has the smallest angle error. The angle error decreases with increasing airgaps however the difference in the angle-error for the OOP sensor is quite insignificant, as can be seen in 6.13b.) for $ag = 3mm$ and $ag = 6mm$, meaning that the solution for an OOP sensor that is somewhat insensitive to offset is utilizing an airgap of around 1mm.

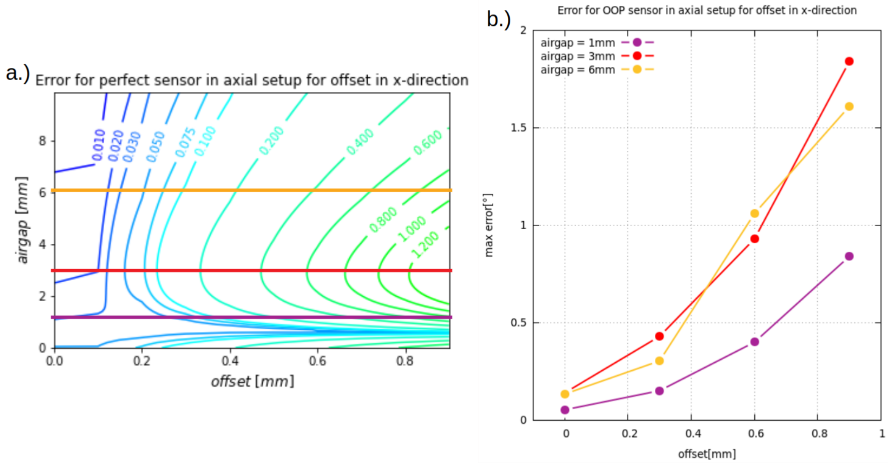

Figure 6.13: a.) The error has been calculated for a sensor which perfectly measures the applied field for varying airgap and offset, i.e a Hall-sensor b.) The error for an OOP-sensor for certain airgaps with varying offset, the colours in the graph were chosen so that they would mach the lines from a.) in order to show the connection between the error of a perfect/Hall sensor and the error of an OOP sensor.

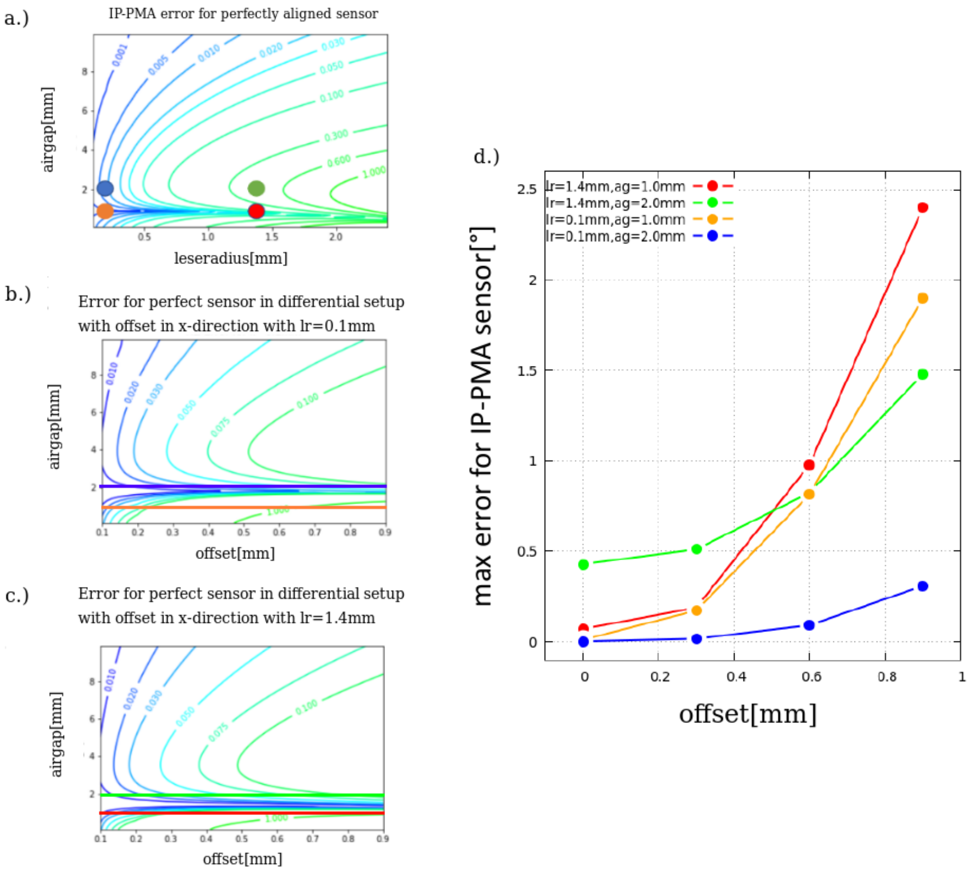

Figure 6.14: a.): Contour plot for the angle error of a perfectly aligned IP-PMA angle-sensor dependent on the leseradius and the airgap, individual positions have been marked with colorized dots. b.): Contour plot for the angle-error the magnetic field gives, or in other words the error a perfect sensor would make, dependent on offset and airgap for $lr = 0.1mm$, lines were drawn to match the colours of the positions for $ag = 1.0mm$ and $ag = 2.0mm$,c.): same as b.) but for $lr = 1.4mm$ d.):Angle error an IP-PMA makes when being offset in the x-direction, the colours of the plots were matched to the colour of the dots in a.) and to the lines in b.) and c.)

,

6.7 Autocalibration

We have now considered a couple of environmental sources of error, an effective method to reduce these is to implement an autocalibration. The basic idea is following, the magnetization signals, which are measured, have the form of a sine- or cosine-function with the same amplitude and a vanishing phase shift, if there are no external errors. However if external errors occur, they alter the individual amplitudes of the magnetization signals and phase shift the signals towards each other, as has been shown in previous sections. Therefore we let the magnet turn one period and we record all the magnetization signals, afterwards we take the maximum $m_{i,max}$ and the minimum $m_{i,min}$, where m_i is one of the magnetization signals, that are needed in order to calculate the angle ϕ, i.e. for the IP sensor $m_i = \{m_{1,z}, m_{2,z}, m_{3,z}, m_{4,z}\}$ and for the OOP sensor $m_i = \{m_x, m_y\}$. We then write

$$a_i = \frac{m_{i,max} - m_{i,min}}{2} \tag{6.18}$$

$$b_i = \frac{m_{i,max} + m_{i,min}}{2} \tag{6.19}$$

$$m_i' = \frac{m_i}{a_i} - \frac{b_i}{a_i} \tag{6.20}$$

obviously a_i is there in order to fix the amplitude and b_i is supposed to realign the phase shift. This autocalibration will not work for every application, however there are plenty of cases where such postprocessing methods are being used. We will now take a look at how this autocalibration works on our different error sources.

Stress induced anisotropy

In a previous chapter we established, that an applied stress will make a significant change in the angle error of the OOP- and Vortex sensors , however not the IP-sensor, as can be seen in figure 6.7. How the stress performs after the autocalibration can be seen in figure 6.15.

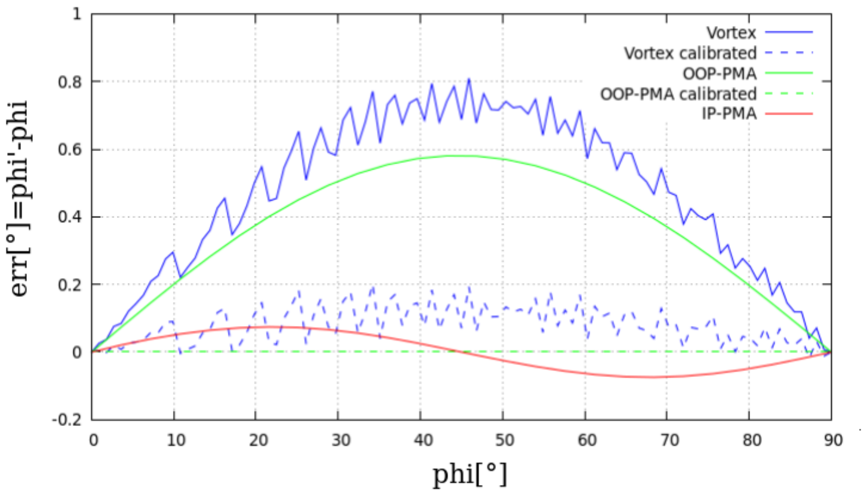

Figure 6.15: An autocalibration has been applied to our results for the angle error of different sensors for $B = 20mT$, where the stress in x-direction induces an anisotropy $k_s = 1.4kJ/m^3$, which causes an external error source.

The error of the Vortex sensor was reduced by a factor of 4 while the error of the OOP-sensor has vanished entirely, meaning that the autocalibration is very effective when it comes to eradicating the errors caused by stress. The IP-sensor has never been effected by the stress induced anisotropy meaning that the autocalibration is of no effect when applied to the IP-sensor.

Bias field

Bias fields increase the angle error of all our sensor concepts in a significant way, if they are applied in the x-direction, why and by how much the angle error gets increased has already been discussed and can be looked up in figures 6.9 and 6.10. Figure 6.16 shows how the autocalibration can help rectify this error source. The error of the Vortex sensor was reduced by a factor of more than 10 while the error which the OOP sensor yields has vanished completely. The magnetization signal of the OOP sensor in the x-direction m_x can be written analogously to the magnetic field in x-direction when a bias field is present

$$m_x = msin(\phi) + m_b \tag{6.21}$$

where m is the amplitude of the magnetization signal and m_b is the bias-magnetization which is caused by the bias field. Applying equations (6.18-6.20) to (6.21) yields

$$m'_x = \frac{msin(\phi) + m_b}{\frac{1}{2}[m + m_b - (-m + m_b)]} - \left[\frac{m + m_b - m + m_b}{m + m_b - (-m + m_b)}\right] = sin(\phi) \tag{6.22}$$

Additionally applying (6.18-6.20) to the magnetization signal in y-direction $m_y = mcos(\phi)$ obviously yields $m'_y = cos(\phi)$. Therefore in theory the error caused by a bias field in x-direction should be reduced by applying such an autocalibration, additionally the case for a bias field in y-direction could be calculated similarly to (6.22), meaning that a bias-field in y-direction would also have no effect on the measured angle ,if such an autocalibration were to be applied.

However the autocalibration does not to seem to be doing much for the IP-sensor. The IP-sensors error stems from the fact that the additional bias makes the transversal field not linear anymore, which cannot be fixed by such a simple autocalibration.

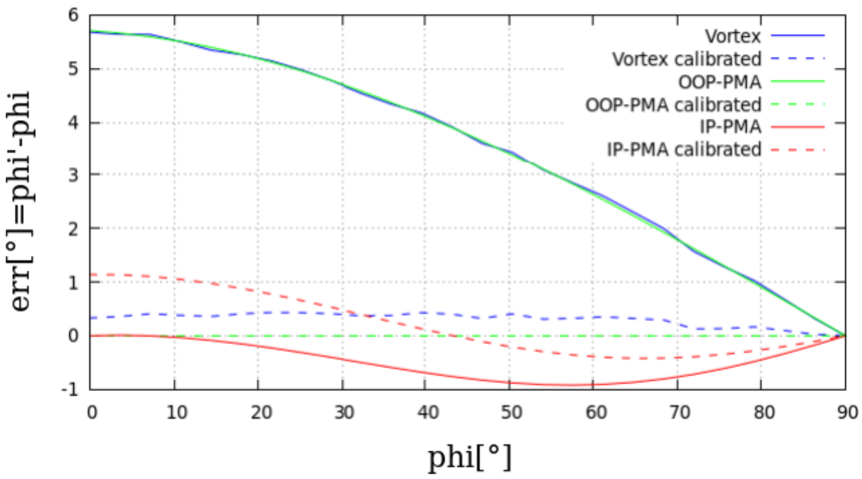

Figure 6.16: An autocalibration has been applied to our results for the angle error of different sensors where a bias-field of $2mT$ in x-direction was applied.

Bibliography

[1] Néel, L. (1954) J. de Phys. et le Rad.52, 225 1954;L. Néel, J. Phys. Radium15, 227

[2] Skomski, R. (2008). Simple models of magnetism. Oxford University Press on Demand.

[3] Abert, C. (2019). Micromagnetics and spintronics: models and numerical methods. *The European Physical Journal B, 92*(6), 120.

[4] Jackson, J. D. (1999). Classical electrodynamics.

[5] Guimarães, A. P., Guimaraes, A. P. (2009). *Principles of nanomagnetism* (Vol. 7). Berlin: Springer.

[6] Becker, R., Döring, W. (2013). *Ferromagnetismus*. Springer-Verlag.

[7] Fernando, G. W. (2008). Magnetic Anisotropy in Transition Metal Systems. In Handbook of Metal Physics (Vol. 4, pp. 89-110). Elsevier.

[8] Gross, R., Marx, A. (2018). Festkörperphysik. Walter de Gruyter GmbH Co KG.

[9] Cullity, B. D., Graham, C. D. (2011). *Introduction to magnetic materials*. John Wiley Sons.

[10] Fraune, M. (2005). *Magnetische Anisotropie und Spintransport in magnetoelektronischen Schichtsystemen und Nanostrukturen* (Doctoral dissertation, Dissertation, II. Physikalisches Institut der RWTH Aachen).

[11] Kittel, C., Galt, J. K. (1956). Ferromagnetic domain theory. In Solid state physics (Vol. 3, pp. 437-564). Academic Press.

[12] E.C.Stoner, E.P.Wohlfarth. (1991) Phil Trans. Roy. Soc. A 240. 599-642. 1948. Reprinted in IEEE Trans. Magn. 27. 3475-3518.

[13] Hubert, A., Schäfer, R. (2008). *Magnetic domains: the analysis of magnetic microstructures*. Springer Science Business Media.

[14] Dzyaloshinsky, I. (1958). A thermodynamic theory of "weak" ferromagnetism of antiferromagnetics. *Journal of Physics and Chemistry of Solids*, 4(4), 241-255.

[15] Moriya, T. (1960). Anisotropic superexchange interaction and weak ferromagnetism. Physical Review, 120(1), 91.

[16] Ruderman, M. A., Kittel, C. (1954). Indirect exchange coupling of nuclear magnetic moments by conduction electrons. *Physical Review*, 96(1), 99.

[17] Lowrie, W. (2007). Fundamentals of geophysics. Cambridge university press.

[18] Bohr, N. (1911). *Studier over metallernes elektrontheori.* Thaning Appel in Komm..

[19] Van Leeuwen, H. J. (1921). Problemes de la théorie électronique du magnétisme.

[20] Ikeda, S., Miura, K., Yamamoto, H., Mizunuma, K., Gan, H. D., Endo, M., ... Ohno, H. (2010). A perpendicular-anisotropy CoFeB–MgO magnetic tunnel junction. Nature materials, 9(9), 721.

[21] Coey, J. M. (2010). Magnetism and magnetic materials. Cambridge university press.

[22] Myers, H. P., Introductory Solid State Physics, 2nd. Ed., Taylor Francis, 1997.

[23] Lenz, J., Edelstein, S. (2006). Magnetic sensors and their applications. IEEE Sensors journal, 6(3), 631-649.

[24] Hirota, E., Sakakima, H., Inomata, K. (2013). Giant magneto-resistance devices (Vol. 40). Springer Science Business Media.

[25] Baibich, M. N., Broto, J. M., Fert, A., Van Dau, F. N., Petroff, F., Etienne, P., ... Chazelas, J. (1988). Giant magnetoresistance of (001) Fe/(001) Cr magnetic superlattices. Physical review letters, 61(21), 2472.

[26] Suess, D., Bachleitner-Hofmann, A., Satz, A., Weitensfelder, H., Vogler, C., Bruckner, F., ... Luber, S. (2018). Topologically protected vortex structures for low-noise magnetic sensors with high linear range. Nature Electronics, 1(6), 362.

[27] Binasch, G., Grünberg, P., Saurenbach, F., Zinn, W. (1989). Enhanced magnetoresistance in layered magnetic structures with antiferromagnetic interlayer exchange. Physical review B, 39(7), 4828.

[28] Anton Bachleitner-Hofmann (2018). Influence of microstructure and geometry on magnetic topology and other properties of mangetoresisitve sensors PhD thesis, Vienna University of Technology

[29] M.Julliere,(1975) Phys. Lett. 54A,225

[30] S.Maekawa and D.Gafvert, (1982) IEEETrans,MAG,MAG-18,707 (1982)

[31] Press, W. H., Teukolsky, S. A., Vetterling, W. T., Flannery, B. P. (2007). Numerical recipes 3rd edition: The art of scientific computing. Cambridge university press.

[32] Newell, A. J., Williams, W., Dunlop, D. J. (1993). A generalization of the demagnetizing tensor for nonuniform magnetization. Journal of Geophysical Research: Solid Earth, 98(B6), 9551-9555.

[33] Donahue, M. J. (1999). OOMMF user's guide, version 1.0 (No. 6376)

[34] Cortés-Ortuno, D., Wang, W., Pepper, R., Bisotti, M. A., Kluyver, T., Vousden, M., Fangohr, H. (2016). Fidimag v2. 0. Zenodo doi, 10.

[35] Berkov, D. V., Gorn, N. L. (2007). MicroMagus–package for micromagnetic simulations. Google Scholar DV Berkov, NL Gorn, http:
www. micromagus. de.

[36] G. Selke, B. Krüger, A. Drews, C. Abert, and T. Gerhardt, (2014) "magnum.fd" https://github.com/micromagnetics/magnum.fd

[37] Paul Thomas Heistracher (2017). Atomistic Spin Dynamics Master thesis, Vienna University of Technology

[38] Yakushiji, K., Saruya, T., Kubota, H., Fukushima, A., Nagahama, T., Yuasa, S., Ando, K. (2010). Ultrathin Co/Pt and Co/Pd superlattice films for MgO-based perpendicular magnetic tunnel junctions. Applied Physics Letters, 97(23), 232508.

[39] Ikeda, S., Miura, K., Yamamoto, H., Mizunuma, K., Gan, H. D., Endo, M., ... & Ohno, H. (2010). A perpendicular-anisotropy CoFeB–MgO magnetic tunnel junction. Nature materials, 9(9), 721.

[40] Muhammad Saleem (2012). Study of Magnetic Features of Nd2Fe14B through the Spin Reorientation Transition by Force Microscopy Magnetic Master thesis, The University of British Columbia

[41] Zangl, H., Faller, L. M., Granig, W. (2017). Optimal design of angular position sensors. COMPEL-The international journal for computation and mathematics in electrical and electronic engineering, 36(5), 1372-1385.

[42] Exl, L., Suess D., Schrefl, T., Micromagnetism - Lecture notes, Source: https://homepage.univie.ac.at/lukas.exl/files/mic_intro.pdf (16:23, 26.11.2019)

[43] Efthimiadis, K. G., Ntallis, N. (2018). Finite element micromagnetic simulation of the magnetic domain structures in thin films with uniaxial anisotropy. Journal of Magnetism and Magnetic Materials, 446, 245-252.